University of Crete

Department of Materials Science and Technology

Plasmonic Organic Photovoltaics

Krassas Miron

University of Crete

September 2015

Supervisors: Prof. Kymakis Emmanuel, Dr. Stratakis Emmanuel, Prof. Kioseoglou Georgios

Abstract

The effects of incorporating uncapped aluminum (Al) nanoparticles (NPs), produced using laser ablation, in the hole transport layer (HTL) of organic photovoltaic devices were systematically investigated. The integration of Al NPs in the poly(3,4-ethylenedioxythiophene):poly(styrenesulfonate) (PEDOT:PSS) hole transport layer resulted in about 9% enhancement in the power conversion efficiency. This improvement can be attributed to a combination of optical and electrical effects. In particular, light trapping inside the photoactive layer takes place due to scattering of the incident light at wide angles by the embedded Al NPs. At the same time, the electrical conductivity of the HTL becomes enhanced, which in effect improves the hole collection and establishes a mobility balance.

Acknowledgements

I would like to express my deepest gratitude to Dr. Emmanuel Stratakis and Prof. Emmanuel Kymakis for the opportunity to carry out this project and their continuous scientific and emotional support. Without their guidance, I could not reach this experience level so soon in my career. My special thanks also to my friend and collaborator George Kakavelakis for his moral support and his knowledge through the difficulties I experienced during the implementation of this work. His guidance also played a vital role in extending my horizon in the field.

Also, I would like to thank Prof. George Kioseoglou for his supervision through the entire year of my thesis work and for the guidance he provided in order to improve expertise.

Finally, I would like to thank the rest of the group, Dr. Costas Petridis, Dr. Minas Stylianakis, Dimitrios Konios, Dr. Naoumis Vaenas, Anna Orfanoudaki and Pavlos Tzourmpakis for their moral support and the friendly environment they provide, each one in his/her one way.

Abbreviations and Symbols

BHJ	Bulk heterojunction
HOMO	Highest occupied molecular orbital
LUMO	Lowest unoccupied molecular orbital
ITO	Indium tin oxide
J_{sc}	Short Circuit current density
LSPR	Localize plasmon resonance
LSPs	Localize surface plasmons
OPVs	Organic Photovoltaics
P3HT	Poly(3-hexylthiophene-2,5-diyl)
PCDTBT	Poly[N-9-hepta-decanyl-2,7-carbazolealt-5,5-(4,7-di-2-thienyl-2,1,3-benzothiadiazole)]
PTB7	Poly[[4,8-bis[(2-ethylhexyl)oxy]benzo[1,2-b:4,5-b']dithiophene-2,6-diyl][3-fluoro-2-[(2-ethylhexyl)carbonyl]thieno[3,4-b]thiophenediyl]
$PC_{71}BM$	Phenyl-C71-butyric acid methyl ester
PCBM	Phenyl-C61-butyric acid methyl ester
PEDOT:PSS	Poly(3,4-ethylenedioxythiophene) poly(styrenesulfonate)
SPPs	Surface plasmon polaritons
TEM	Transmission electron microscopy
V_{oc}	Open circuit voltage
FF	Fill Factor
DCB	Dichlorobenzene
CB	Chlorobenzene
EQE	External Quantum Efficiency
PCE	Power Conversion Efficiency
HTL	Hole transporting layer
ETL	Electron transporting layer
J_{ph}	Photocurrent density

Contents

1. Introduction

The photovoltaic phenomenon was discovered from Alexandre-Edmond Becquerel, a French physicist in 1839. It took 42 years for the first photovoltaic device to appear, an event that triggered the inception of research in a field that nowadays can provide pollutant free energy and ecological solutions. Since that first device, the evolution road of the photovoltaic technology is parted in three generations. The 1st generation was constituted by bulk silicon films, while the 2nd by thin inorganic films. The 3rd generation is divided in two sections, the one that aims cost independently at high efficiencies and the other that aims at low-cost adequate efficiencies. The second part is mainly represented by Organic Photovoltaics (OPVs).

1.1 Motivation

This thesis aims to the manufacturing, characterization and improvement of the performance of Organic Photovoltaic (OPV) devices with the incorporation of metallic nanoparticles (NPs).

A good question to ask is why organic photovoltaics. To answer that, we have to observe the energy productions in countries around the world, which depend mainly on energy resources like gas and petroleum. From the other hand, “modern world” countries use energy resources like uranium and other radioactive materials (nuclear energy). Some of the downsides of those resources are the limited supplies and also the serious negative environmental impact, which extents probably over several future generations.[1]

Renewable energy sources have recently flourished and even introduced to the market, but still they make up a limited part of the total energy production.[2] Exploiting the hydroelectric and wind energy we can produce electrical power. However, the above-mentioned energy transformations are complex, of high cost and require large area facilities.

Geothermal energy is another renewable energy form, which can serve as baseload resource in electrical networks. Geothermal energy can be used as such or convert into electricity. Geothermal energy has a great potential that is already exploited with an increasing rate.

Last but not least, we have the solar energy. The total amount of solar irradiation per year on the Earth's surface equals 1000 times the world's yearly energy needs. Additionally, the direct conversion of solar energy to electricity by the solar cells provides an applicability and potentiality that is absolutely justified.[3]

Nowadays, the majority of solar cells are made by inorganic semiconductors, such as Si and GaAs. The state-of-the-art monocrystalline silicon solar cells can reach power efficiencies up to 27.6% (Fig.1.1). However manufacturing these cells requires many high consuming energy processing steps at very high temperatures leading to relatively high production costs and high energy pay back times (the time required for a solar cell to convert an amount of energy equivalent to that consumed in its production). Hence these solar cells are still too expensive to replace non-renewable energy sources.

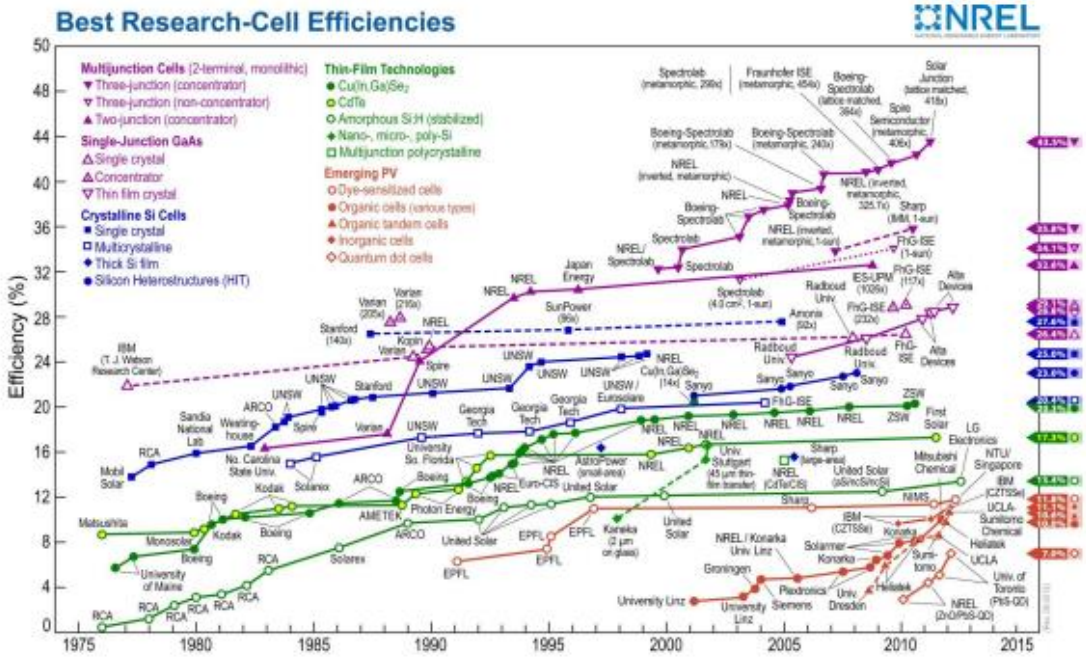

Fig. 1.1 Best research-cell efficiencies for several technologies presented by the National Renewable Energy Laboratory.

On the other hand, organic solar cells with conjugated polymers offer the possibility of low cost, less toxic manufacturing methods and the possibility of large area, light weight, flexible panels. Conjugated polymers are organic molecules with alternating single and double bonds between the carbon atoms and their electrical conductivity ranges from that of insulators to that of metals.

Despite the benefits organic photovoltaics have, they have to fulfill the basic requirements for renewable energy production. The competitive position in the energy market in mainly determined by three factors: efficiency, lifetime and costs. Fig. 1.2 summarizes the restrictions within which organic photovoltaics can be commercialized. Successful commercialization can be realized only if all three technology driving aspects can be fulfilled at the same time.

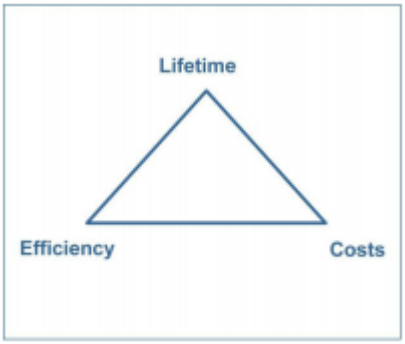

Fig. 1.2 The critical triangle for photovoltaics with the three key factors.[4]

1. World Energy Assessment: Overview,2004 Update, United Nation Development Programme(2004).

2. Renewables in Global Energy Supply, International Energy Agency (2002).

3. A Vision for Photovoltaic Technology Report by the Photovoltaic Technology Research Advisory Council PVTRAC, Directorate General for Research, European Commission (2005).

4. G. Spyropoulos, “DEVELOPMENT AND STUDY OF PLASMONIC ORGANIC PHOTOVOLTAIC CELLS”, Master Thesis.

2. Materials

Currently, several promising, low cost photovoltaic technologies are available and grouped under the name OPVs. All of them have a common, the conversion of the solar energy is accomplished by an organic semiconductor. Therefore, in order to understand the functional mechanism of OPVs, the working principles that govern the organic materials are of high importance.

2.1 Conjugated Polymers

2.1.1 Introduction

Conjugated polymers are a new class of organic materials with promising electronic properties. In their pristine form, their behavior is the same of an insulator or a semiconductor, while in their doped version become conductors. Together with these electrical properties come the intrinsic advantages of polymers, such as low cost, low toxicity and ease of deposit over large area on low weight and flexible substrates. In this section, a short background on conjugated polymers is presented.

The basic element of an organic molecule is carbon, and a polymer contains a long sequence of consecutive carbon atoms. The carbon atoms are in turn linked together by covalent bonds. A polymer chain can be seen as being built up of small units repeating themselves throughout the chain. These units are called monomers and are the building blocks of the polymer. The unique property of conjugated polymers is the presence of conjugated double bonds along the backbone of the polymer. In conjugation, the bonds between the carbon atoms are alternately single and double. Every bond contains a localized σ bond which forms a strong chemical bond. In addition, every double bond also contains a less strongly localized π bond which is weaker.

Firstly, it is essential to understand how the carbon atoms behave when taking part in a chemical bond. The electronic structure of carbon is $1s^2$ $2s^2$ $2p^2$, having six electrons of which only four can be used to establish bonds. The two 1s electrons are referred as core electrons, while the other four electrons are called valence electrons. The valence electrons in the carbon atom exhibit hybridization, a consequence of the electronic excitation of one or more 2s electrons to an empty 2p orbital. Depending on

how the four valence electrons in carbon hybridize, one has sp^3, sp^2 or sp hybridization. In conjugated polymers, three of these electrons, two with 2p ($2p_x$ and $2p_y$) character and one with 2s character, form three sp^2 hybridized orbitals. These three sp^2-hybridized orbitals consist of three lobes, symmetrically directed in the xy-plane. Two of them will form the backbone of σ-bond type, whereas the third will bind to a hydrogen atom. The remaining fourth valence electron will form the p_z orbital pointing normal to the plane of the σ -bonds, as shown in Fig. 2.1; it is delocalized over the whole molecule. The p_z electrons will form π -bonds with the neighboring carbon atoms. This system of interacting p_z-orbitals is called a conjugated π system. The π–electrons can move quite freely a certain distance, which defines the conjugation length. The combination consisting of one of the σ-bonds and one π -bond between two given carbon atoms is referred as a double bond.

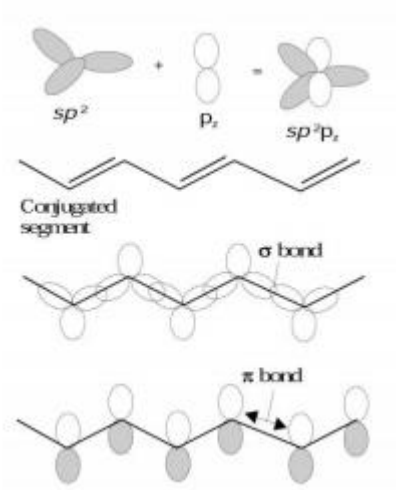

Fig. 2.1 A simple molecular orbital representation of σ and π bonds in trans-polyacetylene, showing the p_z orbitals which overlap to provide the π bonds.

2.1.2 Electronic Properties of Conjugated Polymers

Conjugated polymers are found to be electrical insulated or semiconducting and their bands are similar to those of the inorganic materials. π - bonds of the conjugated polymers are the source of the electrical properties. First, the π -bonds are delocalized over the entire molecule and then, the quantum mechanical overlap of p_z orbitals on two carbon atoms splits their degeneracy and produces two orbitals, a bonding (π) orbital and an antibonding (π^*) (See Fig. 2.2). The lower energy π-orbital produces the valence band, and the higher energy π^* -orbital forms the conduction band. In a

polymer chain, several electrons contribute to the π system and the bonding and antibonding orbitals are made further degenerate, and become broad quasi-continuous energy bands.[5]

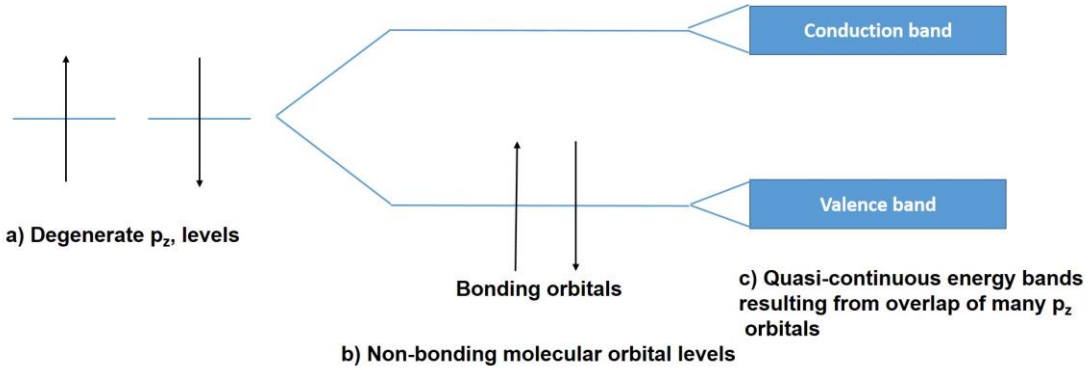

Fig. 2.2 Schematic diagram showing the energy levels of electrons in p_z hybridized atomic levels and subsequently in the π bonding and anti-bonding molecular orbitals when a) two atoms are brought together to form a dimer and b) when a large number of atoms in a chain contribute to the delocalized π system c) further degeneration leads to broad quasi-continuous energy bands

Analogous to the valence and conduction band in inorganic semiconductors, the occupied π band forms the highest occupied molecular orbital (HOMO) and the unoccupied π^* band forms the lowest unoccupied molecular orbital (LUMO) of the polymer. As the overlap between the adjacent p_z orbitals and the number of electrons participating in the π system increases, the widths of the bands become broader, and the energy-gap between them decreases.

The difference in energy between the HOMO and the LUMO is defined as the bandgap. The bandgap controls the optoelectronic properties of the conjugated polymers. Its value varies depending on the geometry and the type of the monomer units building the polymer. Band gaps are in the range of 1.5 to 3.5 eV, indicating that most of the polymers are active in the visible region. Exciting an electron from the valence to the conduction band is equivalent to transferring an electron from a bonding orbital to an anti- bonding orbital, by supplying it with energy greater than this one of the bandgap. In a real polymer chain, the conjugation is unlikely to extend along its full length, as imperfections and defects interrupt the orbital overlap. Instead, there will be a series of chain segments, each of which is characterized by a different

number of repeating units and has a different energy gap. The short chain segments will have a wide energy gap, while the long segments will have a narrow gap.

In solid crystals there is a 3 dimensional electronic band structure corresponding to the 3 dimensional nature of the crystal. Polymers are essentially 1 dimensional systems. That is because of the very long backbone of atoms, strongly bound to each other and the small interaction with neighboring polymer chains. In particular there is strong coupling between the electronic excitations and the local configuration of the polymer chain. This leads to a family of excited states such as solitons, polarons, bipolarons and excitons, which represent the electronic excitations of the polymer combined with their associated lattice distortions.

Excitons

The concept of excitons is well known in the field of semiconductors and molecular crystals but it's a controversy issue in the polymer field. For inorganic semiconductors, the exciton is defined as an electron-hole pair bound by Coulomb attraction (Wannier exciton). In molecular crystals, the exciton can be considered as a bound electron-hole pair localised on one molecular unity (molecular exciton or Frenkel exciton). It is also electrically neutral, with just a dipole moment. When a photon of light of the appropriate energy interacts with an electron in the ground state, the electron is promoted from the HOMO (valence) to the LUMO (conduction) (π-π^* transition). However, the resulting electron and hole are bound, and their motion through the material is coupled. These coupled pairs are known as excitons. An exciton can be considered as a Frenkel exciton, if the pair is confined to one molecular unit or as a Mott-Wannier exciton if it extends over many molecular units.[6] The intermediate case, where the exciton extends over a few adjacent molecular units, can be called the charge transfer exciton. Also, the terms 'inter-chain' and 'intra-chain' exciton are used for polymeric semiconductors to indicate that the constituent charges are located on different or on the same polymer chains respectively. The exciton binding energy of conjugated polymers depends strongly on the structure.[7]

2.2 Polycarbazoles

Polycarbazoles (PCs) result from the polymerization of Carbazoles. Carbazole is an aromatic heterocyclic organic compound. It has a tricyclic structure, consisting of

two six-membered benzene rings fused on either side of a five-membered nitrogen-containing ring. The compounds' structure is based on the indole structure but in which a second benzene ring is fused onto the five-membered ring at the 2–3 position of indole (equivalent to the 9a–4a double bond in carbazole respectively). Low band gap Poly[N-9'-heptadecanyl-2,7-carbazole-alt-5,5-(4',7'-di-2-thienyl-2',1',3'-benzothiadiazole)] (PCDTBT) is one of the most promising high efficient donor materials for OPV devices[8] demonstrating PCEs over than 6% so far and resulting to more stable devices against degradation.[9]

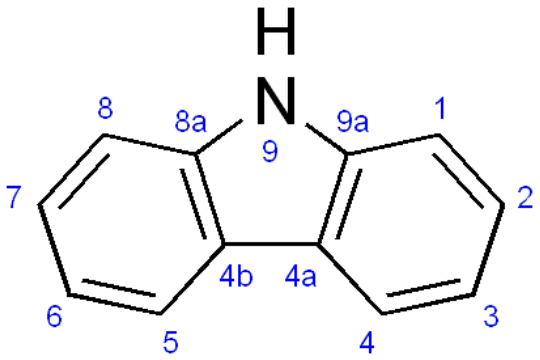

Fig. 2.3 Repeating unit (monomer) of Polycarbazole.[10]

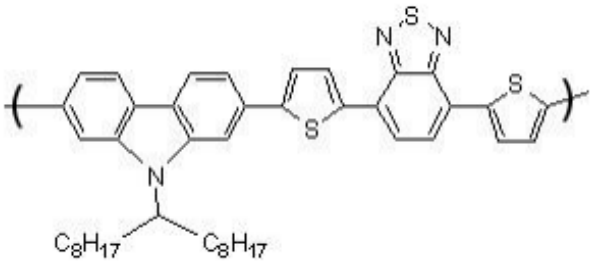

Fig. 2.4 Repeating unit of PCDTBT conjugated polymer.[11]

2.3 Fullerene

Organic materials with appropriate properties, including conjugated polymers and small molecular compounds, can be used as electron donor materials in OPVs. Many organic compounds exhibited potential properties as electron acceptor material, but only a very few electron acceptor materials can be used in highly efficient OPV devices. Fullerene and its derivatives are the most successful electron acceptor materials.

Fullerene C_{60} has well-symmetric structure and exhibits good electron mobility, and as known, one molecule of C_{60} can receive four electrons. Therefore, C_{60} and its derivatives can be used as electron acceptor materials. In 1992, Sariciftci et al. first used C_{60} as electron acceptor and discovered the photoinduced ultrafast electron transfer between electron donor and acceptor.[12] Although, C_{60} can be dissolved in CB and DCB, it exhibits very limited solubility in most of the commonly used organic solvents. In order to improve its solubility and also to avoid severe phase separation of D/A blend, [6,6]-phenyl-C61-butyric acid methyl ester ($PC_{60}BM$) was applied in OPVs. In the past decade, $PC_{60}BM$ and its corresponding C_{70} derivative ($PC_{70}BM$) have been dominantly used as acceptors in OPVs. In comparison with $PC_{60}BM$, $PC_{70}BM$ possesses stronger absorption in visible range, and hence it attracted much interest recently. However, C_{70} is much expensive than that of C_{60} due to its tedious purification process, which limits its application. The molecular structures of $PC_{60}BM$, $PC_{70}BM$ are depicted in Fig. 2.5. $PC_{60}BM$ is crystalline dark-brown powder, and possesses good solubility in common organic solvents such as chloroform, toluene, and o-Dichlorobenzene.[13]

Absorption spectra of $PC_{60}BM$ and $PC_{70}BM$ are depicted in Fig.2.6. It can be seen that both the two materials show strong absorption at ultraviolet region, from 200 to 400 nm, but $PC_{70}BM$ shows stronger absorption in visible region compared to $PC_{60}BM$. Since, OPV devices using $PC_{70}BM$ as acceptor will harvest more sunlight, many OPVs using $PC_{70}BM$ as acceptor show bigger Jsc and hence better PCEs than that of $PC_{60}BM$-based devices.

The electrochemical properties and energy level of the fullerene derivatives is very important for OPVs. The open-circuit voltage (Voc) of OPVs is determined by the difference between the LUMO energy level of the fullerene acceptors and the HOMO energy level of the polymer donors.[14,15] Therefore, the LUMO energy level of the fullerene derivatives is a key parameter for the application of an acceptor to match with a polymer donor. LUMO level of electron donors or acceptors can be measured by cyclic voltammogram (CV) method. LUMO level of unsubstituted C_{60} and PCBM were~ -4.2 and -4.0 eV, respectively.[16,17] Based on the difference of the LUMO levels of those two compounds, it is easy to conclude that LUMO level of C_{60} can be elevated by adding the substituent. As discussed in the above section, higher LUMO level of electron acceptor materials would be helpful to get higher Voc, and for the

purpose to get higher LUMO level, the bisadducts and multiadducts of fullerene were used in OPVs. For example, the LUMO level of bis-PCBM was 0.1–0.15 eV higher than that of PCBM, and when bis-PCBM was used as electron acceptor in P3HT-based OPV device, a Voc of 0.72 V was recorded, which was 0.12 V higher than the PCBM/P3HT-based devices.[18] Furthermore, multiadducts can also be used in OPVs, and higher Voc of the device can be realized. However, since the substituent of PCBM is inert for electron transport and the symmetric property of fullerene can be weakened, electron transport properties of the bis- or multiadducts were not as good as that of PCBM. Therefore, $PC_{60}BM$ and $PC_{70}BM$ are still among the best electron acceptors in OPVs.

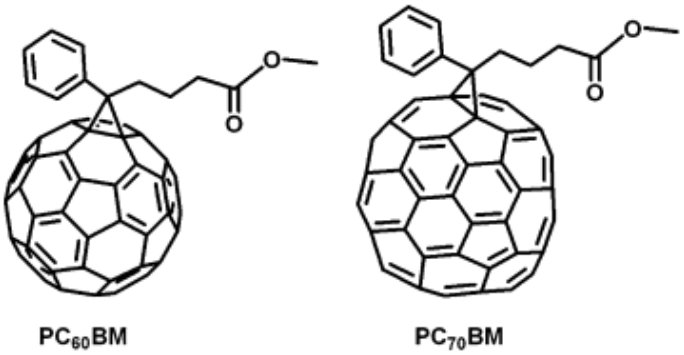

Fig. 2.5 Molecular structures of $PC_{60}BM$ and $PC_{70}BM$.[19]

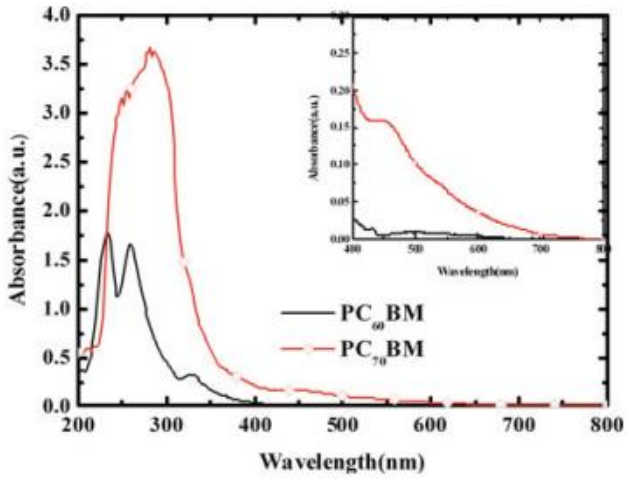

Fig. 2.6 Absorption spectra of $PC_{60}BM$ and $PC_{70}BM$.[20]

2.4 Buffer layer

PEDOT:PSS or Poly(3,4-ethylenedioxythiophene) poly(styrenesulfonate) (Fig. 2.8) is a polymer mixture of two ionomers (Fig. 2.7). One component in this mixture is made up of sodium polystyrene sulfonate which is a sulfonated polystyrene. Part of the sulfonyl groups are deprotonated and carry a negative charge. The other component poly(3,4-ethylenedioxythiophene) or PEDOT is a conjugated polymer and carries positive charges and is based on polythiophene. Together the charged macromolecules form a macromolecular salt.

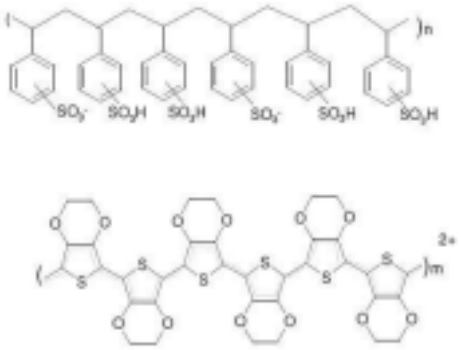

Fig. 2.7 Chemical composition of PEDOT:PSS. The upper region exhibits the oligomer PSS, and the lower region the oligomer PEDOT

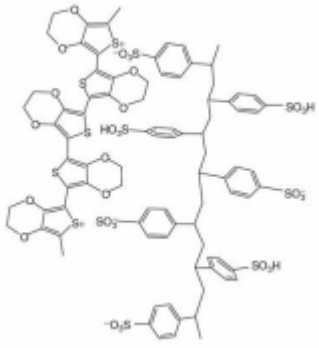

Fig. 2.8 Conformation of PEDOT:PSS

This compound is generally applied as a dispersion of gelled particles in water. A conductive layer on glass is obtained by spreading a layer of the dispersion on the surface usually by spin coating and driving out the water by heat. Special PEDOT:PSS inks and formulations were developed for different coating and printing processes.

Water based PEDOT:PSS inks are mainly used in slot die coating, flexography, rotogravure and inkjet printing. If a high viscous paste and slow drying is required like in screen-printing processes PEDOT:PSS can also be supplied in high boiling solvents like propanediol. Dry PEDOT:PSS pellets can be produced with a freeze drying method which are redispersable in water and different solvents, for example ethanol to increase drying speed during printing. Finally, to overcome degradation to ultraviolet light and high temperature / humidity conditions PEDOT:PSS UV-stabilizers are available.

It is used as a transparent, conductive polymer with high ductility in different applications. These two materials exhibit high transparency (>60%) from 350 to 900 nm. The field of Organic Electronics is one of the fields that utilizes this material exploiting these very interesting characteristics. Furthermore, is reducing the roughness of the ITO layer and optimize the electric contact with the active layer. Additionally, increases the work function of the positive electrode from 4.7-4.9 eV (that fluctuates the work function of ITO) to 5eV.

5. J. J. M. Halls, Ph.D. thesis, Cambridge University, 1997.

6. N. C. Greenham and R. H. Friend, Solid State Physics 49, 1 (1995).

7. S. Mazumbar, M. Chandross, and N. S. Sariciftci, Primary photoexcitations in conjugated polymers (World Scientific, Singapore, 1997).

8. N. Blouin, A. Michaud and M. Leclerc, Adv. Mater., 2007, 19, 2295–2300.

9. Sung Heum Park et. al., Nature Photonics 3, 297 - 302 (2009).

10. https://en.wikipedia.org/wiki/Carbazole

11. http://www.ossila.com/products/pcdtbt

12. Sariciftci NS, Smilowitz L, Heeger AJ, Wudl F (1992) Photoinduced electron transfer from a conducting polymer to buckminsterfullerene. Science 258:1474–1476.

13. Hummelen JC, Knight BW, Lepeq F, Wudl F (1995) Preparation and characterization of fulleroid and methanofullerene derivatives. J. Org. Chem. 60:532–538. doi:10.1021/jo00108a012.

14. Brabec CJ, Sariciftci NS, Hummelen JC (2001) Plastic solar cells. origin of the open circuit voltage of plastic solar cells. Adv Funct Mater 11:15–26. doi:1616-301X/01/0510-0379.

15. Scharber MC, Wuhlbacher D, Koppe M (2006) Design rules for donors in bulk heterojunction solar cells—towards 10% energy-conversion efficiency. Adv. Mater. 18:789 794.doi:10.1002/adma.200501717.

16. Sariciftci NS, Braun D, Zhang C, Srdanov VI, Heeger AJ, Stucky G, Wudl F (1993) Semiconducting polymer buckminster fullerene heterojunctions: diodes, photodiodes, and photovoltaic cells. Appl Phys Lett 62:585–587. doi:10.1063/1.108863.

17. He YJ, Li YF (2011) Fullerene derivative acceptors for high performance polymer solar cells. *Phys Chem Chem Phys* 13:1970–1983. doi:10.1021/ja103275u.

18. Lenes M, Shelton SW, Sieval AB, Kronholm DF, Hummelen JC, Blom PWM (2009) Electron trapping in higher adduct fullerene-based solar cells. Adv Funct Mater 19:3002–3007.

19. https://en.wikipedia.org/wiki/Phenyl-C61-butyric_acid_methyl_ester.

20. G. Kakavelakis, “Device Engineering for enhanced Performance & Stability of Organic Photovoltaics”, Master Thesis.

3 Photovoltaic Technology

3.1 P-N Junction Solar Cells

The heart of solar cell is the semiconductor p-n junction. A standard silicon solar cell consists of a p-doped and an n-doped semiconductor layers forming the p-n junction, an antireflection coating, current collectors and a metal substrate for the collection of photogenerated charge carriers from n-type (electrons) and p-type (holes) layers respectively. A schematic is depicted in Figure 3.1.

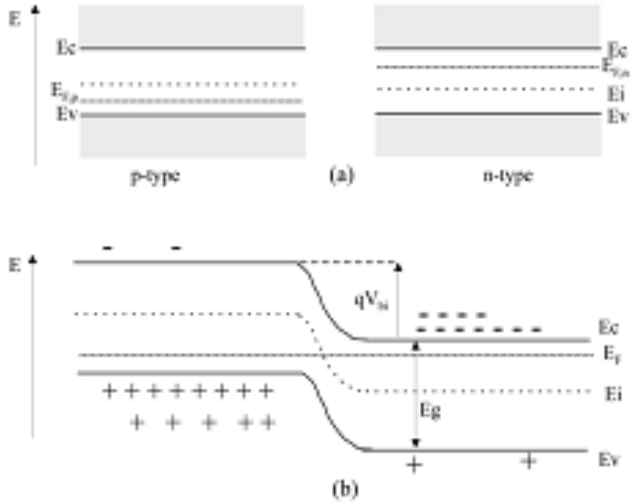

Fig, 3.1 Schematic diagram of a p-n junction, (b) Diagram of energy levels showing creating of a contact potential. While in thermal equilibrium no external voltage is applied between the n-type and p-type material, there is an internal potential, qV_{bi}, which is caused by the work function difference between the n-type and p-type semiconductors.[4]

N-type semiconductors are obtained by doping with impurity atoms having an excess valence electron with respect to the surrounding host atoms, while p-type semiconductors are obtained by doping with impurity atoms with one valence electron less than the surrounding atoms. The n-type doping results in localized energy states just below the conduction band edge of the host semiconductor lattice and occupied by the excess electrons from the impurity atoms, while p-type doping results in (Fig. 3.1) localized empty states with energy slightly above the valence band edge of the semiconductor.

The donor atoms in the n-type material are easily ionized by thermal excitation, due to the closeness of the donor states and the conduction band edge. The ionization

of the donor atoms generates free electrons to the conduction band and leaves empty donor states behind. For the same reason in the p-type material the originally empty acceptor states are partly filled by electrons from the valence band leaving mobile holes to the valence band.

If an n-type and a p- type semiconductor are placed into contact with each other, the Fermi levels of the n ($E_{F,n}$) and p-type ($E_{F,p}$) regions must be aligned, leading to the configuration of Fig 3.1(b). Then the higher concentration of electrons in the n-type material will result in electrons diffusing from the n to the p- type material, and, in a similar way, holes will diffuse from the p to the n-type material. As the electrons diffuse into the p-type semiconductor, they leave behind positively charged atoms causing the n-type semiconductor as a whole to become positively charged. Similarly, as (positively charged) holes diffuse out of the p-type semiconductor, they leave it the p-type material negatively charged.

The result of such a charge motion is that static charges build up in both p-type and n-type materials close to the junction. This charged area is called the depletion region. The charged area forms a potential difference between both materials, inducing a current to flow. This current is called the drift current. It flows in the opposite direction to the diffusion current, and consists of electrons moving from the negatively charged p-type semiconductor towards the positively charged n-type semiconductor. At the same time, holes propagate from positive n-type towards the negative p-type material. Initially the diffusion current dominates the drift current. But as more and more diffusion current flows, the potential causing the drift current builds up, causing larger and larger drift currents until eventually the drift current balances the diffusion current, and they cancel each other. At this point there is no net current flowing between the p-type and n-type regions.

The shift of the bands, which is just the difference between the location of the Fermi level in the n-region and the Fermi level in the p-region, is called the built-in potential, V_{bi}. This built- in potential keeps the majority of holes in the p-region, and the electrons in the n- region. It provides a potential barrier, which prevents current flow across the junction.

The existence of the built- in electric field in the p-n junction region is the source of photovoltaic activity in the cell. Under illumination, a large number of electrons

and holes are generated in the semiconductor material. Minority charge carriers (holes in the n-type and electrons in the p-type layers) generated in the depletion region of the p-n junction, or within their diffusion length from it, are swept to the opposite side of the junction by the built- in electric field of the junction. Under illumination, electrons are therefore accumulated in the n-type material and holes in the p-type material, generating voltage between the opposite sides of the p-n junction and electrical contacts attached to them, as well as current through an external load attached between the contacts.

3.2 Polymer solar cells

3.2.1 Types of OPVs

Nowadays, there are three different types of organic solar cells using organic molecules: «Dye-sensitized nanocrystalline TiO2 solar cells», «molecular organic solar cells» and «polymer solar cells». The higher efficiencies between these types of solar cells (11%) are reported for «Dye-sensitized nanocrystalline TiO2 solar cell», which operates under photo-electrochemical principles. Originally discovered by Gerischer and Tributsch,[21] but named by M.Gratzel,[22] who reported efficiencies in the order of 11% using TiO_2 nanocrystals to achieve large areas interface with electrodes.

Molecular organic solar cells exploit organic dyes. The active layer is deposited by vacuum evaporation techniques. Organic dyes have a high absorption coefficient and an absorption spectrum similar to the solar. However, efficiencies are limited by the small diffusion length of excitons and the small charge mobility in materials. Efficiencies of around 1% achieved already in 1986 by Tang, using copper-phthalocyanine and a perylenetetracarboxylic derivative.[23] Manipulating with C_{60} could slightly improve efficiency. Recently, the use of doped pentacene, which indicates higher mobility carriers, increased efficiency up to 2 % for thin films and 4.5 % for monocrystalline provisions.[24]

The third type of organic solar cells, the «polymer solar cells», is to be analyzed extensively since is the topic of this thesis. The original «polymer cells», which consisted of one polymer layer enclosed between two asymmetric contacts, demonstrated low efficiencies due to insufficient charge generation in polymer layer. The discovery of photoinduced charge transfer from a pi-conjugated polymer to a

fullerene opened new avenues for organic photovoltaics and LEDs. This process is done with almost no deviations since it is much faster than any competitors, radiant or not, path "relaxation." Bilayer devices with conjugated polymers and C_{60} fullerenes demonstrated improved efficiencies. But only the light absorbed within the distance of diffusion length of excitons in interface contributed to the current.

Sudden revolutionary progress in «polymer solar cells» welcomed with the introduction of bulk heterojunction concept. Stirring conjugated polymer with C_{60}, or a more soluble fullerene derivative, led to a three dimensional heterojunction with the ability to generate efficiently charge throughout the layer. Very soon, efficiencies up to 1% could be achieved. The morphology and improvement of interfaces between the electrical contacts are critical for the efficiency of the device. Intensive polymer engineering and improving of contacts led to a rise of the efficiencies close to 9 %.

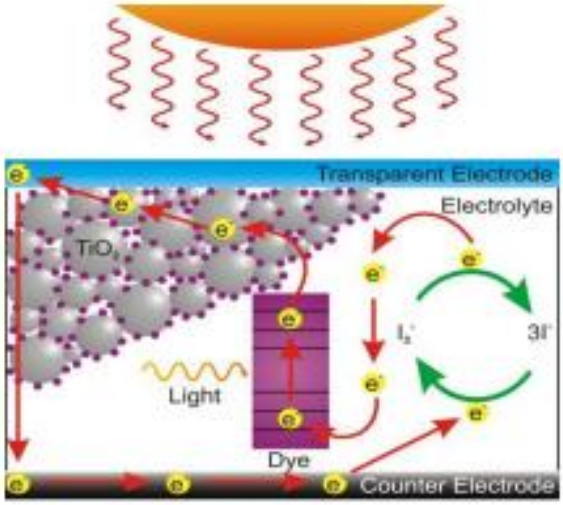

Fig. 3.2 Dye-sensitized solar cell.[25]

3.2.2 Bulk heterojunction concept and operating principles

Basic principles

These are the three fundamental steps that take place during the light conversion into electricity by a photovoltaic cell:

(i) Light absorption

(ii) Charge carriers generation

(iii) Selective transport of opposite charges on opposite contacts.

The generic operating principles are the same for all photovoltaic cells, but a description for a BHJ cell of polymer-fullerene dispersion should be done. This type of solar cell consists of a mixture of polymer-fullerene (or derivative) disposed between two planar electrodes as shown in Fig. 3.3. An ITO layer deposited on glass serves as a transparent electrode of high work function, while a thin layer of metal, such as aluminum, is used as the electrode with the low work function.

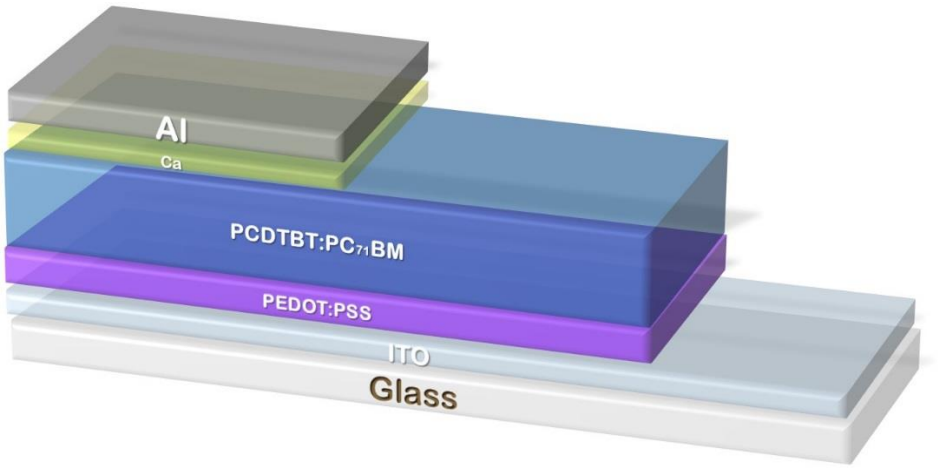

Fig. 3.3 Bulk heterojunction concept solar cell

The production of a photocurrent in an organic cell of this type, in which the built in field (in rough analogy to a p-n junction) is provided by the difference in work functions of the electrodes, arises from the following phenomena (Fig. 3.4)

Fig. 3.4 Conversion steps of an organic solar cell.

As reported previously, the photogeneration mechanism in organic semiconductor materials is very similar to that encountered in an inorganic p–n cell. A photon with energy hω greater than the energy gap E_g can excite an electron from π to π* orbital (HOMO-LUMO excitation). This will form an exciton, which should be splitted to provide a hole at one electrode (anode) and an electron at the cathode (i.e., to start the production of photocurrent). The exciton is separated at the interfaces of polymer-

fullerene. We conclude that the absorption of light is directly associated with the short circuit current (I_{sc} for V = 0). The absorption spectrum and the thickness of the active substrate are important parameters. The thickness can not be increased above a certain limit due to the limited carrier mobility.

Charge generation occurs at the interfaces or in a p-n junction or a Schottky diode type interface. As a p-n junction can be considered the mixture of polymer-polymer or polymer- fullerene, while Schottky diode is defined as semiconductor-metal interface. Only light that is absorbed in the collapse region of the interface or in the radius of the exciton diffusion length can generate free carriers.

The transfer of photoinduced charge (the electron) from conjugated polymer to fullerene is an effective way to generate carriers. The photoinduced charge transport at the interface polymer-fullerene occurs in times of the order of 15 fs. This process is much faster than any radiative or non-radiative decay or electrons in conjugated polymer.

Charge transport occurs in a procedure that follows several steps as it shown in figure 3.5. D and A are donor and acceptor, respectively. Indicators 1,3 indicate the singlet and triplet excited states.

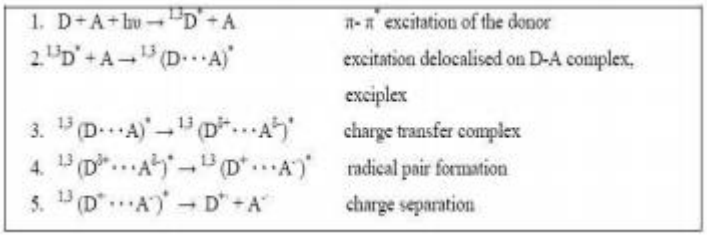

Fig. 3.5 Serial reaction for an ultra-fast electron transport from a donor (p-conjugated polymer) to an acceptor (fullerene derivative). The corresponding hole transfer from a donor to an acceptor follows the same procedure

Thermodynamic principles dictate that the potential needs the excited donor (electron) to ionized (I*D) is less than the sum of electron affinity of the acceptor with Coulomb interaction between the separated conditions of charge.

$$I_D^* - A_A - U_C \leq 0$$

I_D^* can be estimated from the inverse electronic affinity. That means that the LUMO of the donor is higher than the LUMO of the acceptor, neglecting Coulomb interactions.

During the third step, the charges that have been generated are selectively transferred to the electrodes. The holes 'jump' from fullerenes to polymers until they reach ITO, while the electrons propagate from polymers to fullerene until Al contact. The conjugates polymers exhibit high charge mobility longitudinally to the chain, but the mobility is limited by the dialysis between the chains. Certainly, there are some factors for the efficient separation and collection of carriers, such as the association between the fullerene in the mixture, the crystallinity of the polymer, the dispersion of fullerene and will be discussed later.

Bulk heterojunction solar cell

A bulk heterojunction solar cell consists of an active organic part with a donor and an acceptor material, the metal electrodes and the substrate. The substrate is responsible for mechanical stability (for glass substrate). Usually the substrate is transparent, so the light will first pass through it before reaches the active material. The substrate is usually made by glass, but it could also be a transparent plastic. The positive electrode in our device is made usually by indium tin oxide (ITO). The cathode is made by aluminum. The aluminum electrode is thick enough to reflect the unabsorbed light back into the device. Both electrodes have the task to transport the charges from the organic material to the electrical contacts with minimal losses. The electrodes' work functions can be optimized for electron and hole extraction to selectively design a quality diode. If the work functions do not match, it is possible to introduce an additional layer between the electrode and the organic material to adjust the work functions of the different materials. That's one of the tasks for PEDOT:PSS for the hole and the Ca for the electron extraction. Also, intermediate layers can block the transport of holes or electrons towards the anode and the cathode respectively.

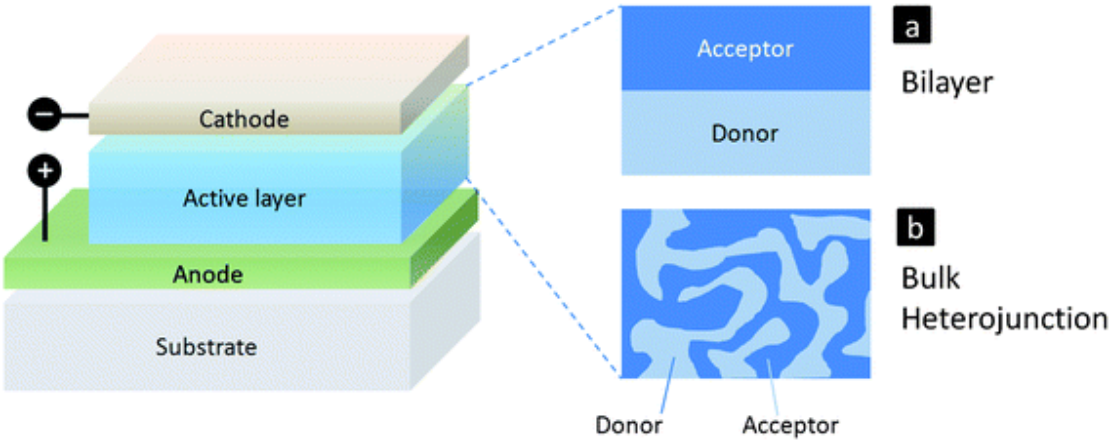

Fig. 3.6 Schematic diagrams of a) bi-layer heterojunction and b) bulk heterojunction photoactive layer.[26]

Finally, in the center of the solar cell, the organic part is present. The organic donor and acceptor materials have different electron affinities, which means that the acceptor material rather receives electrons than donates. Whereas the donor material prefers to release electrons. The acceptor material in this work was the PCBM. PCDTBT was the donor material. The donor is the material in a BHJ that absorbs the majority of the incident light in the solar cell.

If the incoming photon has an equal or higher energy than the optical bandgap in the absorber material, then there is a probability for the photon to be absorbed. The optical bandgap is defined by the difference of the band levels of the highest occupied molecular orbital (HOMO) and lowest unoccupied molecular orbital (LUMO) of the absorber material (PCDTBT). If the photon is absorbed, an exciton is generated. An exciton is a quasi-neutral particle and contains a positive and negative charge. An exciton can diffuse maximum 20nm during its lifetime.[27] If the exciton does not reach the donor acceptor interface it will recombine, and the absorbed energy is converted into thermal energy or a photon is emitted and thus cannot be used for electric current generation. If the exciton reaches the interface it can dissociate, with the electron transferring to the acceptor material. Some energy is lost due to the difference in the LUMO levels of the donor and acceptor material. The generated charges are driven by drift and diffusion to the electrodes, where they are free to move through the external circuit.

In inorganic solar cells the absorber material has a small dielectric constant (ε_{Si} = 11). From Coulomb's law, $F=(1/4\pi\varepsilon_{Si})q_1q_2/r^2$, the force keeping the pair electron-hole (exciton) together is stronger compared to the organic absorber material (ε_{PCDTBT} = 3). In OPV devices, an acceptor and a donor material is needed to generate free charges. In a pure absorber material, excitons would be generated but not separated and therefore no photon-generated charges should be noticed. In this case excitons can only be split at impurities.

Taking into account that the diffusion length of an exciton is approximately 20 nm, the donor and acceptor material should interpenetrate each other in the nanometer scale, to keep a low probability for the recombination of the exciton. The separated charges also have a lifetime. If the thickness of the film is too large, the charges will recombine before they reach the electrodes. Therefore, the thickness of the device is limited by the mobility of the carriers in the organic semiconductor. In thin devices, on the other hand, many photons are not absorbed. Thus, there is an optimum to find, between high absorption rate and low recombination rate for separated charges. The system can be optimized by increasing the carrier mobility[28] and the optical absorption coefficient of the materials.

3.3 Characteristics of a photovoltaic device

3.3.1 Current-Voltage Characteristics

The light absorbed in the junction creates electron-hole pairs whose concentration is proportional to number of absorbed photons with energies larger that the energy gap (E_g) of the material. These electrons and holes are separated by the built-in electric field and are responsible for the production of an electric current, I_L, called the light-generated current. By neglecting the recombination effect in the depletion region and including the effect of generation in this region, I_L can be expressed as follows:

$$I_L = qA\int_0^w G(x)dx, \textbf{ (1)}$$

Here G(x) is the generation rate of the electron-hole pairs, A is the device area, and w is the width of the depletion region. The direction (and, hence, the sign) of the

light-generated current is opposite to the direction of the dark current, which can be calculated by the following equation:

$$|I_{dark}| = I_s \left[\exp\left(\frac{V}{nkT}\right) - 1\right], \textbf{(2)}$$

whereas I_s is the saturation current of the diode, q the elementary charge, n the diode ideality factor, k the Boltzmann constant and T the temperature. If the light generated current is larger than the dark current, the device acts as a current source, that is, as a source of electricity. Then, the total diode current under illumination is given by the Shockley equation:

$$I = I_L - I_s \left[\exp\left(\frac{V}{nkT}\right) - 1\right], \textbf{(3)}$$

where, as customary for solar cells, we chose the sign of the light-generated current to be positive. As can be seen from the above equation, setting I to zero, the ideal value of the open circuit voltage, V_{oc}, of a solar cell is given by:

$$V_{OC} = \frac{kT}{q} \ln\left(\frac{I_L}{I_s} + 1\right), \textbf{(4)}$$

The built-in electric field separating the electrons and holes generated by light can at most provide the built-in potential, V_{bi}. Hence, the built- in voltage gives the upper bound of the open circuit voltage. The effect of the parasitic series and shunt resistances, R_S and R_{SH} due to device bulk resistivity and presence of defects can included in the Shockley equation as:

$$I = I_s \exp\left(\frac{q}{nkT}(V - IR_S) - 1\right) + \frac{V - IR_S}{R_{SH}} - I_L, \textbf{(5)}$$

Figure 3.7 depicts the equivalent circuit of p-n junction solar cell, in which the I-V characteristic is described by the equation above (see equation (5)). The circuit consists of the following three parts. A current source I_L that takes into account the light-generated current, a diode that accounts for the nonlinear voltage dependence and a shunt as well as a series resistors.

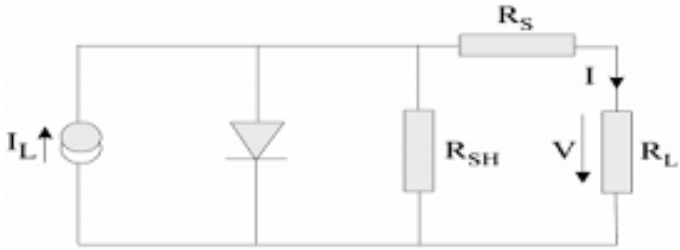

Fig. 3.7 Equivalent circuit of a p-n junction solar cell

The current source generates a current I_L up on illumination. I_L can be described as the number of free electron/hole pairs immediately after generation - before any recombination takes place. The series resistance R_S is due to the bulk resistance of the semiconductor material, the bulk resistance of the metallic contacts and the contact resistance between the metallic contacts and the organic semiconductor. The shunt resistance R_{SH} is caused by leakage across the p-n junction around the edge of the cell and in non-peripheral regions in the presence of defects and precipitates of foreign impurities in the junction region.

In conclusion, in the standard p-n junction solar cell, light absorption occurs via band gap excitation of electrons in the bulk of the semiconductor, charge separation in the internal electric field of the p-n junction and charge collection by transport of electrons and holes through the bulk of the semiconductor to the electrical contacts.

3.3.2 Solar cell efficiency

Respectively the net current density is given by

$$J(V) = J_{SC} - J_{dark} = J_{SC} - J_0 \left[\exp\left(\frac{qV}{k_B T}\right) - 1\right], \textbf{(6)}$$

where J_S is the short-circuit current density and J_{dark} the current flowing under no illumination described by the ideal Shockley diode equation.

It is common to use I-V characteristics to indicate the efficiency of solar cells. The open-circuit voltage Voc and the short-circuit current Isc are determined by a given light level by the cell properties. The open circuit voltage can easily be derived from equation 7 given that there is no net current flowing:

$$V_{OC} = \frac{k_B T}{q} \ln\left(1 + \frac{J_{SC}}{J_0}\right), \textbf{(7)}$$

An expression for the photocurrent density at short circuit can be given by

$$J_{SC} = q \int_0^{\infty} a(E)\eta_{coll}(E)[1 - R(E)]\Phi(E)d\lambda$$

$$= q \int_0^{\infty} EQE(E)\Phi(E)d\lambda, \textbf{(8)}$$

where Φ(E) is the incident spectral photon flux density and R(E) the fraction of reflected photons as a function of the photon energy. α(E) and η_{coll}(E) are the absorption coefficient and collection efficiency of the solar cell material, respectively. The product α(E) x η_{coll}(E) x [1- R(E)] is known as the external quantum efficiency and reflects the probability of an incident photon generating one electron that is collected at the contacts. The EQE does not depend on the incident spectrum, hence it is therefore a key quantity in describing solar cell performance under different conditions.

The maximum power delivered to a load by a solar cell occurs when the product V I gives its maximum value, P_m, i.e. when the solar cell operates at its maximum voltage (V_m) and maximum current density (J_m). The fraction of maximum power and the product of V_{oc} and J_{sc} is defined as the fill factor, FF (Figure 3.8), which further can be related to the efficiency, η.

$$\eta = \frac{J_m V_m}{P_S} = \frac{J_{SC} V_{OC} FF}{P_S}, \textbf{(9)}$$

where Ps is the incident light power input from the sun.

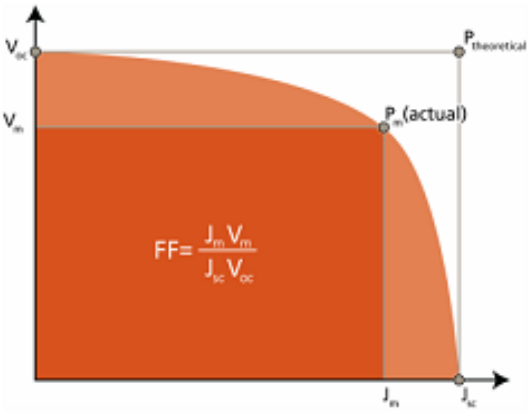

Fig. 3.8 Current-voltage characteristics and the fill factor of a solar cell.[20]

21. Gerischer, H. Tributsch, H. Ber. Bunsen-Ges. Phys. Chem. 1968, 72, 437-445.

22. Brian O'Regan, Michael Grätzel (24 October 1991). "A low-cost, high-efficiency solar cell based on dye-sensitized colloidal TiO2films". Nature 353 (6346):737–740.

23. Tang, C. W., Two-layer organic photovoltaic cell, Applied Physics Letters (1986), 48(2), 183-5.

24. H. Kim, J. Lee, S. Ok and Y. Choe, "Effects of pentacene-doped PEDOT:PSS as a hole-conducting layer on the performance characteristics of polymer photovoltaic cells", Nanoscale Res Lett. 7, 5, 2012

25. http://www.geog.ucsb.edu/events/department-news/723/inventor-of-dye-sensitizedsolar-cells-awarded-millennium-technology-prize/

26. Prashant Sonar, Jacelyn Pui Fong Lim and Khai Leok Chan, "Organic non-fullerene acceptors for organic photovoltaics", Energy Environ. Sci., 2011, **4**, 1558.

27. H. Hoppe and N. Sariciftci, "Organic solar cells: An overview," J. Mater. Res., vol. 19, pp. 1924{1945, 2004.

28. J. Nakamura, K. Murata, and K. Takahashi, \Relation between carrier mobility and cell performance in bulk heterojunction solar cells consisting of soluble polythiophene and fullerene derivatives," Appl. Phys. Lett., vol. 87, p. 132105, 2005.

4 Light trapping by different mechanisms

4.1 Plasmons

Metal nanoparticles have been used as decorative pigments since the time of the Romans when it was discovered that silver and gold particles in the nano range embedded in dielectric surroundings exhibit unique optical properties.[29] The most famous example is maybe the Lycurgus Cup from the 4th century AD. Analysis have shown that the glass contains small amounts of nanoparticles of silver and gold approximately 70 nm in diameter. The cup appears green in the reflected light and looks red when a light is shone from inside and is transmitted through the glass as seen in figure 4.1. This is due to the excitation of surface plasmon modes on the gold and silver particles embedded in it.

Fig. 4.1 The Roman Lycurgus cup from the 4th century AD in (a) reflected light and (b) transmitted light.[30]

The energy of the surface plasmon resonance depends on the dielectric constants of both the nanoparticle and the surrounding medium. Mie was the first to explain the red color of colloidal gold nanoparticles in 1908, after Michael Faraday had stated in 1831 that particle size was the color-determining factor.[31,32] Mie's biggest discovery was that materials which real part of the dielectric function was negative, showed an anomalous peak in the absorption spectrum in form of small particles.[33]

The reduction of the dimensions of materials has pronounced effects on the optical properties. The reason for this behavior can generally be ascribed two different phenomena. One is due to the quantum confinement, i.e. increased energy level spacing as the system becomes more confined, and the other is related to the surface plasmon resonance.

Metallic photonic materials demonstrate unique properties due to the existence of electro-magnetic surface waves known as surface plasmons. Surface plasmons are set to become part of the photonics revolution in which the interaction between light and matter is controlled by producing patterned structures that are periodic on the scale of the wavelength of light. Surface plasmons open up a wealth of new possibilities for photonics because they allow the concentration and propagation of light below the usual resolution limit, thus opening up such possibilities as sub-wavelength optical components.

4.1.1 Basic introduction to plasmons

Plasma is a medium which has equal concentrations of positive and negative charges, from which one of them has the ability to move. Plasmons are quanta of plasma oscillators and they are related to materials with metallic properties. This material in equilibrium conditions has the mobile negative charges stabilized by fixed positive ions. This is known as the jellium model in metals. Now if these conditions were disturbed by an electromagnetic field, a non-uniform charge distribution will be formed and hence an internal field will be generated. The negative charges will gain momentum, but since the pulled back from the positive charges, they end up oscillating about the positive charge distribution. This oscillation is called a plasmon.

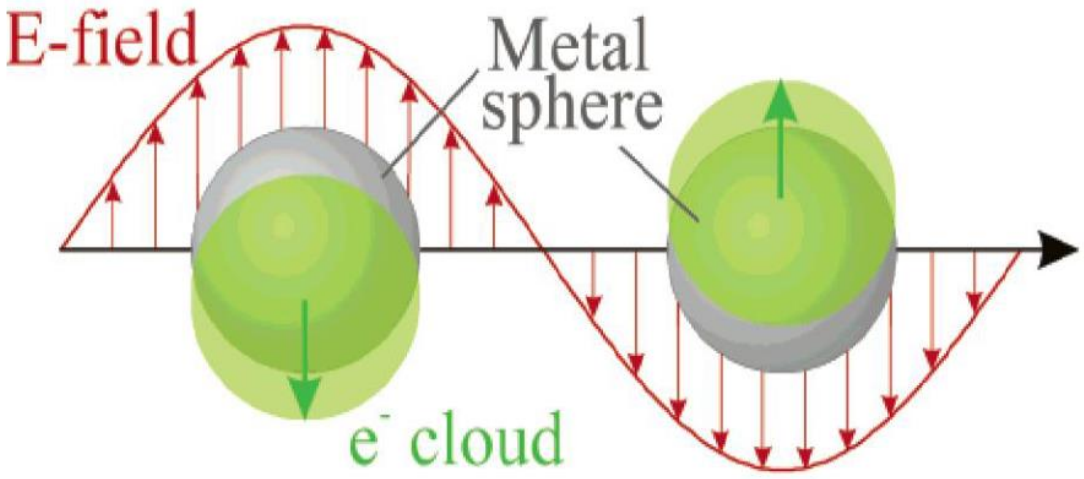

Fig. 4.2 Schematic of the plasmon oscillation of a sphere, showing the displacement of the conduction electrons relative to the nuclei.

4.1.2 Bulk, Surface plasmons and Surface plasmon polaritons

Bulk plasmons

When considering plasmons that exist in the bulk, one can think of longitudinal oscillation of free electrons in an infinite metallic medium. The frequency of this oscillation called plasma frequency, ω_p, and is given by the equation[34]

$$\omega_p = \sqrt{\frac{ne^2}{\varepsilon_0 m}}, \textbf{ (10)}$$

where n is the electron density, e the electron charge, m the electron mass and ε_0 the permittivity of free space. Bulk plasmons contribute in different way from the surface plasmon in the optical properties of solids. This due to the small effect the energy of the visible light has to the momentum of the electrons, which reduces the probability of plasmon excitation. The conduction electrons will simply relax back to equilibrium conditions when using visible wavelengths.[6]

Surface plasmons

SPs are transverse, but they are mismatched to photons in their momentum. They have an associated electromagnetic wave with both transverse and longitudinal field components. Such waves can only be excited at the interface between a conductor and dielectric, and are tightly bound to the surface. The fields reach their maximum at the

interface (z=0), and exponentially decay away from the surface. The wave-vector of the surface plasmon mode (k_{spp}) always lies to the right of the free space wave-vector (k_0), such that $\lambda_{spp} < \lambda_0$, where λ_{spp} is the wavelength of the surface plasmon and λ_0 is the wavelength of light in free space (vacuum). Additionally, this makes it impossible to directly launch a surface plasmon wave by illumination with free-space radiation: the free-space photons simply do not have enough momentum to excite the surface plasmon.

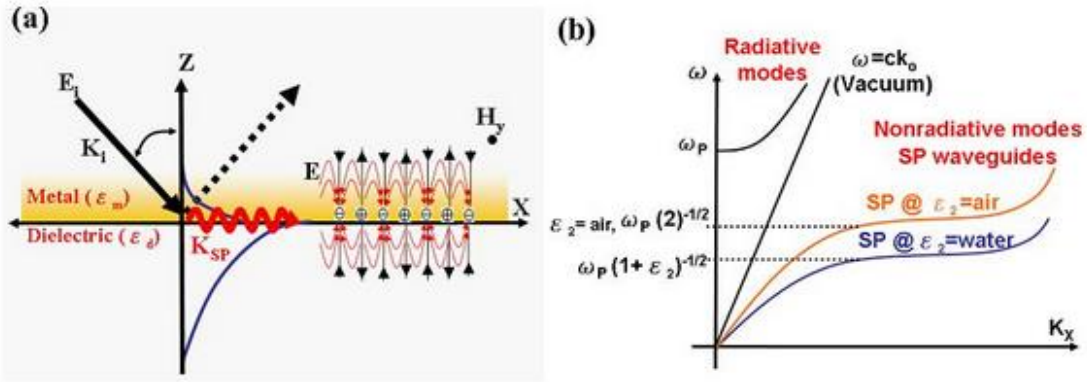

Fig. 4.3 Schematic presentation of surface plasmons is constituted of resonantly oscillating surface charges at a metal/dielectric interface and of the electromagnetic surface wave that originates from these surface charges. (a) Electric field lines of a surface plasmon on a smooth surface and the electromagnetic field of SPs propagating on a surface in the x direction. (b) The dispersion relation of non-radiative SP modes and radiative modes.[35]

The frequency, ω_{sp}, of a surface plasmon on the flat surface of a nearly infinite piece of metal, can easily be determined from the frequency of a bulk plasmon in a metal, ω_p, because it corresponds to: Re $\varepsilon_m^*(\omega_{sp}) = -\varepsilon_i$, where $\varepsilon_i > 0$ is the dielectric constant of the dielectric medium. By solving the equations given for the dispersion relationship and the dielectric function, the maximum frequency of the surface plasmon is found to be:

$$\omega_{sp} = \frac{\omega_p}{\sqrt{1+\varepsilon_d}} = \frac{\omega_p}{\sqrt{2}}, \textbf{(11)}$$

for a metal with free electrons in contact with a vacuum medium. As ω increases, k_{spp} gets larger and larger, moving further away from k_0. As k_{spp} increases, the surface plasmon wavelength decreases and the wave is more tightly bound to the surface. This process has an upper limit of ω_{sp}, the surface plasmon resonant frequency, which

occurs when the dielectric constant of the metal and the dielectric have the same magnitude but opposite signs.

A surface plasmon is an electro-magnetic wave propagating along the surface of a thin metal layer. SPs are coherent delocalized electron oscillations that exist at the interface between any two materials where the real part of the dielectric function changes sign across the interface (e.g. a metal-dielectric interface, such as a metal sheet in air). The total excitation, including both the charge motion and associated electromagnetic field, is called either a surface plasmon polariton at a planar interface, or a localized surface plasmon for the closed surface of a small particle.

SPs have lower energy than bulk (or volume) plasmons which quantise the longitudinal electron oscillations about positive ion cores within the bulk of an electron gas (or plasma). Optical excitation of the surface plasmon can be achieved in the so-called Kretschmann configuration[36], where p-polarised, collimated light beam undergoes total internal reflection at a glass/thin-metal-film/dielectric interface. The angle at which the resonance occurs is extremely sensitive to any change in the refractive index (RI) of the medium adjacent to the metal surface, and such changes can be monitored by recording intensity of reflected light when the system goes out of resonance. The concept of surface plasmons originates in the plasma approach of Maxwell's theory: the free electrons of a metal are treated as an electron liquid of high density (plasma) and density fluctuations occurring on the surface of such a liquid are called plasmons, surface plasmons (SP), or surface polaritons [H. Raether, "Surface Plasmons", Springler-Verlag, Berlin, 1988.].

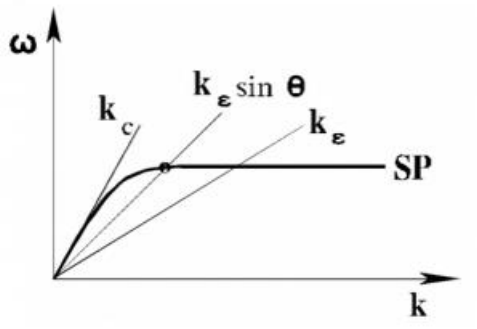

Fig. 4.4 Frequency (ω)-wave vector graph (k) and Surface plasmons.[37]

According to Maxwell's theory[38], surface plasmons can propagate along a metallic surface and have a spectrum of Eigen frequencies (ω) related to the wave-vector (k) by a dispersion relation:

$$k_{SP} = \sqrt{\frac{\varepsilon_1 * \varepsilon_2}{\varepsilon_1 + \varepsilon_2}}, \textbf{(12)}$$

$\varepsilon_2 = \varepsilon_2' + i\varepsilon_2''$ and $\varepsilon 1$ are the dielectric constant of the metal and of the medium in contact with it, respectively. Wave vector k_1 of light at frequency ω travelling through the medium ε_1 is described by:

$$k_1 = \frac{\omega}{c} * \sqrt{\varepsilon_1}, \textbf{(13)}$$

where c is the speed of light in vacuum, and for vacuum (or air to some approximation) its dispersion relation is a straight line $k_1=\omega/c$ (line kc in figure above). Since the SP's dispersion relation (curve SP in figure above) never intersects the dispersion relation of light in air, they cannot be excited directly by a freely propagating beam of light incident upon the metal surface. However, it is possible to "turn down" the light line to the point where both lines cross each other.

4.2 Surface plasmon polaritons (SPPs)

Because of the long-range nature of the organizing forces in plasma oscillation, in small systems it is reasonable to expect that the electrons will sense the presence of the boundaries and modify their collective behavior accordingly. Indeed, surface plasmons are possible in thin film, propagating along the interface of a conductor and dielectric medium where the real part of dielectric function, ε, has opposite signs.[39] Analogous to bulk plasmons, these plasmons are restricted to the mobile electrons of surfaces. When the excitation of these plasmons is combined with that of a photon, a surface plasmon polariton is created. Two important properties of SPPs must be considered related to the photon-excitation of plasmons: First, there is a momentum mismatch between the polariton and the photon. Second, the electromagnetic field created by the oscillations has its peak at the surface and will decrease exponentially while the distance from the surface increase.[40,41] Special techniques must be used to match up the light into the plasmons and we can say that SPPs are non-radiative waves on the surface.

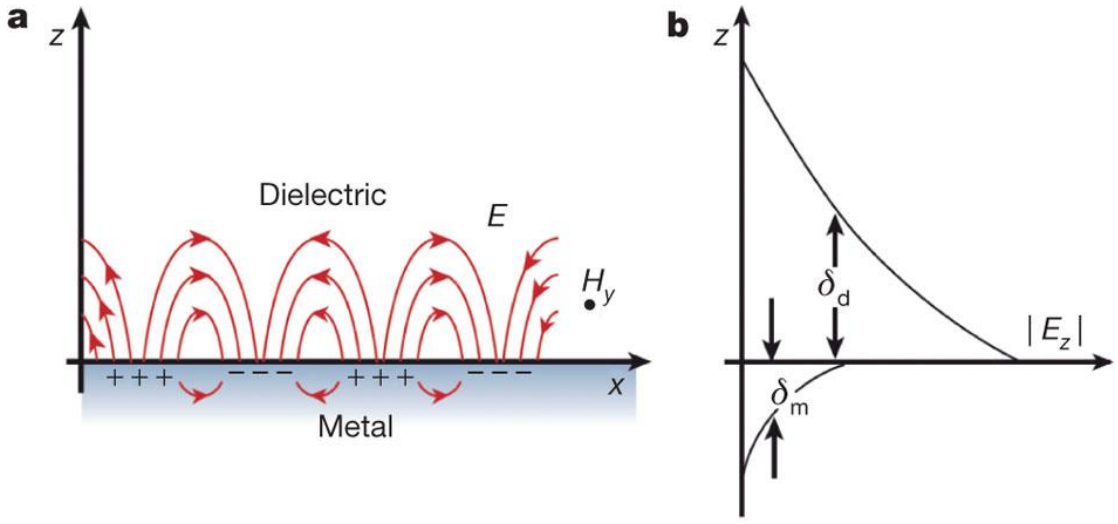

Fig. 4.5 The electric field perpendicular to the surface is enhanced near the surface and decays exponentially with distance away from it (a). This field is said to be evanescent, reflecting the bound surface plasmon modes and prevents power from propagating away from the surface (b)[42]

At flat metal surfaces, excitations can only be achieved in the metal-dielectric interface by use of special geometries that provides the required wavevector, k_{sp}, matching the surface wave with that of the light producing it.[43,44]

SPPs have higher j-values which means higher momentum (hk) than the light of the same frequency. This leads to a stronger interaction between oscillating electrons and the electromagnetic field of light, which again results in unique optical properties. To understand this, we need to take a look at the surface plasmon dispersion relation derived from the Maxwell equations under appropriate boundary conditions.

$$k_{sp} = k_0 \sqrt{\frac{\varepsilon_m \varepsilon_d}{\varepsilon_m + \varepsilon_d}}, \textbf{(14)}$$

where the free space vector is k_0=w/c and ε_m and ε_d the dielectric constants of the metal and the dielectric medium, respectively. The dielectric constant of the metal is frequency dependent and given by the Drude formula[45]

$$\varepsilon(\omega) = 1 - \frac{\omega_p^2}{(\omega^2 + i\gamma\omega)}, \textbf{(15)}$$

where ω_p is given by equation (10) and is the collision frequency of the electrons usually termed the damping coefficient. Then, to get the surface plasmon k vector larger than that of light, the square root in equation (14) must be larger than (10). This is obtained when ε_m and ε_d have different signs. A metal will directly satisfy this

criterion since its ε_m is negative and complex. As a result of the higher momentum of SPPs than light, power will be prevented from propagating away from the surface. This is the fundamental principle behind surface plasmon waveguiding.[46]

On the flat surface of a nearly infinite metal, the frequency, ω_{sp}, of a surface plasmon can be determined from the frequency of a bulk plasmon in a metal, ω_p, because it corresponds to: Re $\varepsilon_m(\omega_{sp}) = -\varepsilon_i$ where $\varepsilon_i > 0$ is the dielectric constant of the dielectric medium. Solving the equations for the dispersion relationship and the dielectric function, the maximum frequency of the surface plasmon is found to be

$$\omega_{sp} = \frac{\omega_p}{\sqrt{1+\varepsilon_d}} = \frac{\omega_p}{\sqrt{2}}, \textbf{ (16)}$$

for metal in contact with vacuum medium. Once a surface plasmon is excited by light on a flat surface of the metal, it will propagate but also gradually degrade because of losses arising from absorption in the metal. The degree of degradation depends on the dielectric function of the metal at the frequency at which the surface plasmon oscillates. Most often, the surface plasmon resonance frequency ω_{sp} lies in the UV (ultra-violet) region for metals and the IR (infra-red) region for heavily doped semiconductors.

4.3 Localized surface plasmons (LSPs)

If we consider a metal surface with curvature or roughness and hence more confinement to the geometries that the surface plasmons are bound to, it will give rise to a different kind of plasmon excitation. Different from SSPs, localized surface plasmons (LSPs) are confined to curved metal objects, such as small metal particles or voids in metallic structures. These LSPs are characterized by frequencies which depend upon the size, shape and dielectric constant of the object to which the plasmon is confined. SPP modes can only be excited if both the frequency and wavevector of the exciting light match that of the SPP. In contrast, LSPs can be excited resonantly with light of appropriate frequency (and polarization), independent of the excitation light wavevector.[47]

LSPs are also assigned to features on metal surfaces. For them to be excited, the geometry to which they are confined needs to be finite and within a certain size. Different size and shapes can affect the intensity as well as the peak-shift of the

scattering produced by the particles or surface features. The LSPs effect is valid if the dimension of the system is smaller than the wavelength of the exciting light. In a small metal particle, the negative charges are moving by the influence of an external field while the cations are assumed to be fixed. This external field will give rise to a displacements of both charges. If the incoming light is treated as constant, the problem can be treated with electrostatics rather than electrodynamics, the approximation is said to be quasistatic. This electric field, E(t), on a nanoparticle with dimensions much smaller than the wavelength of the light creating it with dielectric constant ε_m, induces a dipole moment,[48]

$$\vec{p}(t) = \varepsilon_0 \varepsilon_m a\vec{E}(t), \textbf{ (17)}$$

where ε_0 and ε_m is the dielectric constant in vacuum & in the metal nanoparticle respectively and a is the polarizability of the particle. The internal field is given by[45]

$$E_i = E_0 \frac{3\varepsilon_d}{\varepsilon_m + 2\varepsilon_d}, \textbf{ (18)}$$

where ε_d is the relative permittivity of the dielectric medium and ε_m is the relative permittivity of the particle, $\varepsilon_m = \varepsilon'_m + i\varepsilon''_m$. The real term describes the polarizability and the imaginary the absorption. The imaginary term can be directly related to the absorption coefficient, $a=4\pi k/\lambda$.[44] Materials with negative values for the ε'_m have high reflectance and small dissipation. Metals has this property below the bulk plasma frequency, and this is the reason for their high reflectivity.[47] The polarization, a, of a sphere can be found by,

$$a = 3V\varepsilon_0 \frac{\varepsilon_m - \varepsilon_d}{\varepsilon_m + 2\varepsilon_d}, \textbf{ (19)}$$

as given by Mie. The dielectric constants are given before and V is the volume of the particle. The polarization is at the largest when $\varepsilon_m = -2\varepsilon_d$ or $|\varepsilon_m + 2\varepsilon_d|$ is at its minimum. The solution to this is the frequency where $\varepsilon' = 2^{\varepsilon_m}$ and $\varepsilon'' = 0$ (Frölich frequency).[47] From equation (18), at the same frequency, we have the same strong interaction of the spheres with the field. This frequency corresponds to the surface plasmon resonance, and is given by

$$\omega_{lsp} = \frac{\omega_p}{\sqrt{1+2\varepsilon_d}}, \textbf{ (20)}$$

for a metal sphere in vacuum (ε_d=1, $\omega_{sp}=\omega_p/\sqrt{3}$). In case of voids in the bulk of a metal, the frequencies of both of them (with the same shape) can be estimated from each other as they are related like

$$\omega_{\text{part}}^2 + \omega_{\text{void}}^2 = \omega_{\text{p}}^2, \textbf{ (21)}$$

Since LSPs is confined to a particle, it can result to a photon absorption, scattering and a significant enhancement of the electromagnetic field when the volume to which it is localized gets very small. Enhancements 2-4 magnitudes the magnitude of incident field has been observed in the proximity of the metal nanoparticles and with a spatial resolution of 10-50 nm. The spectrum of the LSPs depends on the size and shape of the nanoparticles, the distances between them and the dielectric properties of the surroundings substrate and medium.

4.4 Light scattering

The incident light scatters in all different directions. The intensity of the scattered light depends on the polarizability of the particle. This property of light scattering makes it a valuable tool for measuring molecular weight.

Light scattering is another method of light trapping. The interaction of light with matter can reveal important information about the structure and dynamics of the material being examined. Because the intensity of scattered light depends on molecular weight of the particle, light scattering will depend on weight average molecular weight. This result contrasts to colligative properties, such as osmotic pressure, which only depended on number of particles and therefore gave the number average molecular weight. Besides molecular weight dependence, light scattering also has a direct dependence on particle size. For polymer solutions, this dependence on size can be used to measure the radius of gyration of the polymer molecule. As with osmotic pressure, we expect all light scattering experiments to be done in non-ideal solutions. No ideality complicates the data analysis, but, like osmotic pressure, allows you to determining a virial coefficient, A2. In summary, light scattering experiments can be used to measure three things: weight average molecular weight ($\overline{M_W}$), mean-squared radius of gyration $\langle\langle s^2\rangle\rangle$, and the second virial coefficient (A2 or Γ2).

To interpret light scattering experiments, we begin with a discussion of light scattering theories. Classical light scattering theory was derived by Lord Rayleigh and is now called Rayleigh theory.[49,50] Rayleigh theory applies to small particles. By small particles, we mean particles whose size is much less than the wavelength of the light that is being scattered. By "much less" we mean:

$$\sqrt{\langle s^2 \rangle} < \frac{\lambda}{20}, \textbf{ (22)}$$

Because visible light has λ between 4000˚A and 8000˚A, we need the root mean squared radius of gyration $\sqrt{\langle s^2 \rangle}$<200 to 400 Å. Many polymers will violate this criterion and the light scattering results will have to be corrected for large particle size effects.

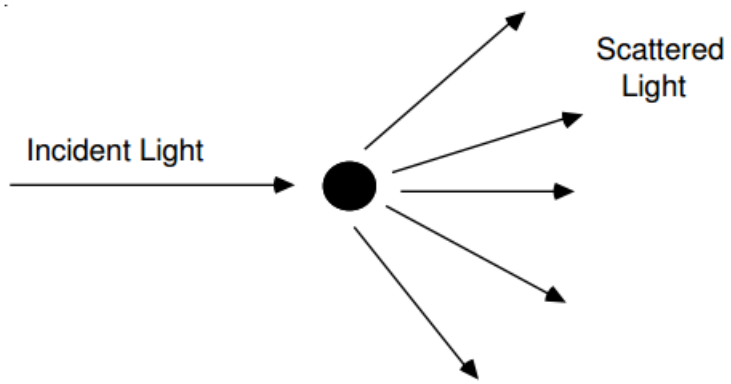

Fig. 4.6 Scattering of incident light off a particle in solution.

A light scattering theory known as the Rayleigh-Gans theory was developed to extend Rayleigh theory to particles that are not "optically" small. The correction method involves extrapolation techniques that expand light scattering intensity to zero scattering angle. This correction technique is important for analyzing results on polymer solutions. Analysis of osmotic pressure experiments requires extrapolation techniques to account for non-ideal solutions. In light scattering there are two non-ideal effect — non-ideal solutions and large particle size effects. Thus, analysis or deconvolution of light scattering data requires two extrapolations. One is an extrapolation to small particle size to remove the large particle size effect. The other is an extrapolation to zero concentration to remove the effect of non-ideal solutions. The slope of the first extrapolation gives the mean squared radius of gyration $\langle\langle s^2 \rangle\rangle$.

The slope of the second extrapolation gives the second virial coefficient (A2). The intercept of the two extrapolations gives the weight average molecular weight ($\overline{M_W}$).

From the strong dependence upon the radius of the particle, it seems like the scattering efficiency will increase with the particle size. This is indeed true for particles within a certain order of size. NPs dispersed into the photoactive layer of OPV devices can offer a major enhancement on its optical absorption, either via the formation of scattered waves at the large diameter NPs or due to excitation of LSPR modes at the smaller diameter NPs[51]. As an example, Al NPs (10-70 nm) act as an effective ‘‘optical reflector’’ and multiple reflections will cause solar light to pass multiple times through the BHJ layer.

Extinction by metal nanoparticles

By the word extinction, we mean the sum of the absorption and scattering of the incident light by the metal nanoparticles. Ideally we prefer scattering processes, since most of the energy absorbed by the nanoparticle is lost into heat.[52] When the frequency of the incident radiation is in the range of the surface plasmon resonance, the polarizability of the particle increases and the field lines affects more strongly in a larger distance from the particle. The result is that light may interact with the particle over a cross-sectional area larger than its geometrical cross-section. The former can be defined from the following equations

$$C_{abs} = \frac{2\pi}{\lambda} \mathrm{Im}[a], \textbf{(23)}$$

$$C_{scat} = \frac{1}{6\pi}\left(\frac{2\pi}{\lambda}\right)^4 |a|^2, \textbf{(24)}$$

where a is the polarizability of the particle, given by

$$a = 3V\frac{\varepsilon_m - \varepsilon_d}{\varepsilon_m + 2\varepsilon_d}, \textbf{(25)}$$

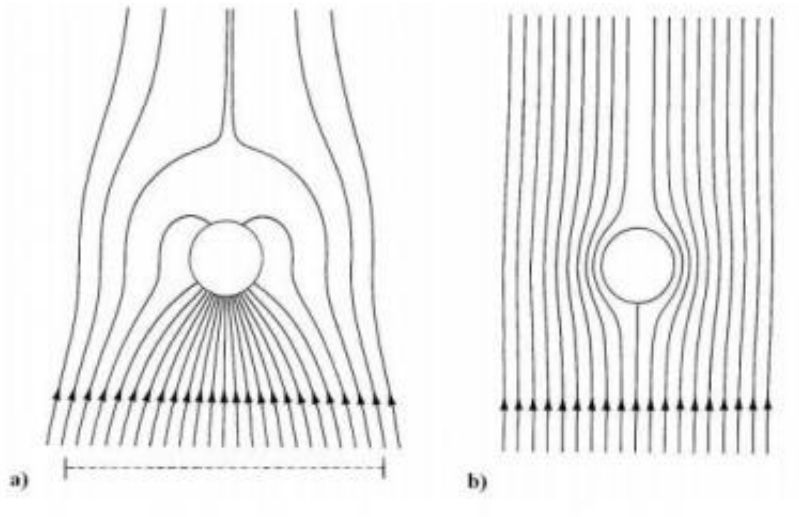

Fig. 4.7 Field lines around a small aluminum sphere illuminated by light of energy 8.8eV (a) and 5eV (b). The dashed, horizontal line represents the effective radius of the sphere for absorption of light.[39]

Fig. 4.7 depicts the field lines of the overall electric field vector around a small Al sphere illuminated by light of energy 8.8 eV and 5 eV. The result: an 18 times greater absorption cross-section than the geometrical cross-section of the particle in the case of 8.8 eV, which is characteristic energy of the surface plasmon in aluminium.

A scattering efficiency, Q_{scat}, can be defined as the ratio between the scattering and the geometrical cross-section.

$$Q_{scat} = \frac{C_{scat}}{\pi r^2} = \frac{9}{8} r^4 \left(\frac{2\pi}{\lambda}\right)^4 \left|\frac{\varepsilon_m - \varepsilon_d}{\varepsilon_m + 2\varepsilon_d}\right|^2, \textbf{(26)}$$

Another popular term is the radiative efficiency Q_{rad}, which is the scattering efficiency divided by the total extinction. It is beneficial for understanding the relative significance of the processes for e.g. certain particle sizes and at certain wavelengths.

Because of the strong dependence upon the particle radius, it seems like the increase of the particle size will increase the scattering effect. This is true for a certain order of size. Based on photocurrent measurements from metal islands of different size on SOI (silicon-on-insulator) devices, a string size-dependence was observed on the scattering intensity of the particles.[53] Larger nanoparticles have increased effective cross-section due to larger polarizabilities and radiative efficiencies. Thereby increased interaction between the particle and the incident light. From the other hand,

in small nanoparticles, absorption dominates the extinction process in the material. As the particles grow larger, scattering processes will prevail until it reaches a certain size where the external electric field is no longer able to polarize the whole particle homogeneously. The result is the excitation of higher order plasmon modes (quadrupole, octopole) and radiation damping which will constitute important corrections to the quasistatic expressions given for the polarizability and cross-sections. For particles larger than the wavelength, a large fraction of the light will be reflected rather than excite plasmons.[54]

Size and shape of the particles

The decrease of the particle sizes induce limitations to the mean free path of the electrons due to the particle boundaries.[55] This will result in a sharpening of the absorption peak, and as the particles grow larger they generally show a stronger resonance peak because of the increased extinction cross-section, but no significant shift of the resonance frequency is observed.[56] When the particles grow beyond a certain diameter depending on the dielectric properties of the material, the resonance peak will broaden and shift to lower energies because of retardation effects and the excitation of higher order multipoles. These multipole excitations are observed as shoulders or distinct peaks in absorption spectra.[57.58.59]

Experiments on nanospheres lithography with silver nanoparticles shown that the normalized extinction can be tuned from the UV region to the far IR (4000 nm) by varying the size and shape of the nanoparticles.[60,61] Both red-shift and broadening of the absorption peak would be an advantage for solar cell applications, since light trapping should happen over an extended spectrum and especially at ranges were silicon absorbs poorly. Even though an increase of the size results to a large absolute scattering cross-section, it is in fact lowered when normalized by size.

4.5 Nanoparticles in OPVs

In OSCs, enhancement of the absorbance of a polymer film of a specific limited thickness still remains a challenge. A major hindrance toward the development of OPVs is the fundamental tradeoff between light absorption and collection of photo generated excitons. Efficient charge transport in BHJ OPVs is provided that

continuous pathways for both charge carriers exist. Naturally, the presence of such pathways is less likely for thicker active layers. In addition, carriers exhibit reduced exciton diffusion lengths in organic semiconductors due to limited hopping transport.[62] As a result, active layer thicknesses in optimized OPV devices are small, typically around 200 nm. Owing to such a low active layer thickness, the best devices that have been developed absorb poorly, despite displaying low charge–carrier recombination. Research in this area has indicated that the compromise between efficient light harvesting and efficient charge collection, determined by the organic layer thickness, can be resolved by 'trapping' incident light in the active layer. One promising plasmon enhanced light-trapping approach is the utilization of plasmonic metallic nanoparticles (NPs). Either between interfaces, or inside the buffer or the active layers of OPV devices in order to promote absorption, thereby increasing the optical thickness of OPV materials for light harvesting.[63,64]

Noble metallic NPs (Ag, Al, and Au) are known to exhibit a strong absorption band in the UV–Vis region, which lies within the optical absorption band of the conjugated polymers used in the active layer of OPVs. The physical origin of this enhanced absorption is the coherent oscillation of the free electrons (free electrons in metal: $n \approx 1023\ cm^{-3}$), coined as a plasmon wave, which is excited by the incident electromagnetic field.[65] When the electron cloud is displaced relative to the nuclei, a restoring force arises from Coulomb attraction between electrons and nuclei that results in an oscillation of the electron cloud relative to the nuclei framework. NPs with dimensions well below the wavelength of light in the quasi-static limit, exhibit scattering and absorption cross-sections depending on the NP diameter.

The exploitation of the plasmonic effect, that accompanies metal NPs, has been proved a successful strategy in order to enhance the light absorption and thus the efficiency of organic photovoltaics (OPV).[66] The spatial arrangement of metal NPs in the vicinity of the OPVs photoactive medium meet the trade off the high charge collection and high light absorption. Depending on the NPs size the absorption cross section (sub-wavelength antennas) increases or the optical path (scattering centers) extends within the photoactive medium(Fig. 4.8).

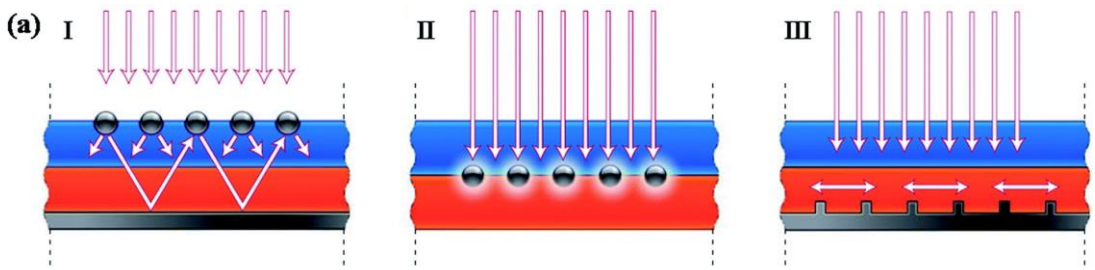

Fig. 4.8 Different geometries for plasmonic light trapping in thin-film solar cells - (a) scattering from metal nanoparticles into high angles in the semiconductor, causing increased optical path lengths in the cell. (b) The near-field of the excited metal nanoparticles causes the direct generation of electron-hole pairs. (c) Excitation of surface plasmon polaritons at the metal/semiconductor interface ensures the coupling of incident light to photonic modes propagating in the semiconductor layer plane.[67]

Specifically, when the NPs diameter is smaller than 40 nm, NPs act as sub-wavelength antennas, leading to enhanced light absorption due to plasmon resonance effect.[68] Larger diameter NPs function as multiple scattering centers, giving rise to increase of the optical path length within the photoactive medium.[69] Even through the NPs attach advantages in the OPVs active medium or the buffer layers, their exploitation is not absent of drawbacks including: carrier recombination, exciton quenching between the active materials and metallic NPs, induction of unfavorable film morphology, disturbance of phase distribution of D:A and therefore depression of the exciton separation and lowering of the OPVs efficiency.

29. Luis M. Liz-Marzán. Nanometals: Formation and color. Materials Today, 7:26–31, 2004. 29, 61, 114, 115.

30. Tim Kelf. Surface plasmon polaritons. 7, 29.

31. Kenneth Klabunde. Nanoscale Materials in Chemistry. Wiley-Interscience, First edition, 2001. 29.

32. Guozhong Cao. Nanostructures & Nanomaterials - Synthesis, Prpoerties & Applications. Imperial College Press, 57 Shelton Street, London, UK, 2004. 29.

33. Uwe Kreibig and Michael Volmer. Optical properties of metal clusters. Springer, 1995. 29, 30, 37.

34. Charles Kittel. Introduction to Solid State Physics. John Wiley and Sons, New York, Chichester, seventh edition, December 1996. 30.

35. http://www.intechopen.com/books/advances-in-graphene-science/graphene-oxide-based-surface-plasmon-resonance-biosensors.

36. http://www.ncbi.nlm.nih.gov/pubmed/22832550.

37. http://www.bionavis.com/technology/spr/.

38. http://www-ssc.igpp.ucla.edu/personnel/russell/papers/max_mag.

39. Harry A. Atwater and Albert Polman. The optical properties of metal nanoparticles: The influence of size, shape, and dielectric environment. MRS Bulletin, 30(3):385–389, 2005. 31.

40. Harry A. Atwater and Albert Polman. The optical properties of metal nanoparticles: The influence of size, shape, and dielectric environment. MRS Bulletin, 30(3):385– 389, 2005. 31.

41. Luis Prill Sempere. Surface plasmon polaritons (spp) and their use in subwave-length optics. Term paper for Physics of Nanostructures. 31, 32.

42. Oliver Benson, "Assembly of hybrid photonic architectures from nanophotonic constituents", Nature 480, 193, 2011.

43. Paras N. Prasad. Nanophotonics. Wiley-Interscience, 2004. 31.

44. Andreas Otto. Excitation of no radiative surface plasma waves in silver by the method of frutrated total eflection. Zeitschrift für Physik A, 216:398–410, 1968.31.

45. Craig F. Bohren and Donald R. Huffman. Absorption and scattering of light by small particles. John Wiley and Sons, Inc., Weinheim, Germany, 1983. 7, 31, 33, 34, 35, 36, 37, 73, 109, 115, 119.

46. Stefan A. Maier, Paul E. Barclay, Thomas J. Johnson, Michelle D. Friedman, and Oskar Painter. Low-loss fiber accessible plasmon waveguide for planar energy guiding and sensing. Appl. Phys. Lett., 84(25):3990– 3992, 2004. 32.

47. Anatoly V Zayats and Igor I Smolyaninov. Near-field photonics: surface plasmon polaritons and localized surface plasmons. Journal of Optics A: Pure and Applied Optics, 5(4):S16, 2003. 32, 33.

48. David Blazquez Sanchez. The Surface Plasmon Resonance of Supported Noble Metal Nanoparticles: Characterization, Laser Tailoring, and SERS Application. PhD thesis, The University of Kassel, Germany, 2007. 33.

49. http://www.globalspec.com/reference/13974/160210/chapter-2-rayleigh-theory-and-mie-theory-for-a-single-scatterer.

50. http://www.ias.ac.in/initiat/sci_ed/resources/chemistry/LightScat.pdf.

51. J. Y. Lee and P. Peumans, Opt. Express, 2010, 18, 10078.

52. Leung Tsang, Jin Au Kong, and Kung-Hau Ding. Scattering of electromagnetic waves: Theories and applications. Wiley-Interscience, 2000. 33.

53. Martin Green. Silicon Solar Cells - Advanced Principles & Practice. Centre for Photovoltaic Devices and Systems, UNSW, Sydney, N.S.W. 2052m, Australia, 1995. 33.

54. Supriya Pillai. Surface plasmons for enhanced thin-film silicon solar cells and light emitting diodes. PhD thesis, School of photovoltaic and renewable energy engineering, University of New South Wales, Australia, 2007. 8, 33, 51, 52.

55. Craig F. Bohren and Donald R. Huffman. Absorption and scattering of light by small particles. John Wiley and Sons, Inc., Weinheim, Germany, 1983. 7, 31, 33, 34, 35, 36, 37, 73, 109, 115, 119.

56. F. J. Beck and K. R. Catchpole. Red-shifting the surface plasmon resonance of silver nanoparticles for light trapping in solar cells. In Mater. Res. Soc. Symp. Proc.Vol., volume 1101. Materials Research Society conference, San Francisco, 2008.36, 37, 40

57. K. L. Kelly, E. Coronado, L. L. Zhao, and G. C. Schatz. The optical properties of metal nanoparticles: The influence of size, shape, and dielectric environment. J Phys Chem B, 107:668–677, 2003. 7, 30, 36

58. Jack J. Mock, David R. Smith, and Sheldon Schultz. Local refractive index dependence of plasmon resonance spectra from individual nanoparticles. Nano Letters,3(4):485–491, 2003. 36, 37

59. Johanna Jacoba Penninkhof. Tunable plasmon resonances in anisotropic metal nanostructures. PhD thesis, Utrecht University, Netherlands, 2006. 33, 36, 37, 38, 4156. R. H. Ritchie. Plasma losses by fast electrons in thin films. Phys. Rev., 106(5):874–881, Jun 1957. 34.

60. V. Shrotriya, et al. Appl. Phys. Lett. 88 (2006) 064104.

61. E.T. Yu, J. van de Lagemaat, MRS Bull. 36 (2011) 424.

62. H.A. Atwater, A. Polman, Nat. Mater. 9 (2010) 205.

63. W.L. Barnes, et al. Nature 424 (2003) 824.

64. E. Stratakis, E. Kymakis, Mater. Today 16 (2013) 133–146.

65. H. A. Atwater & A. Polman, Nat. Mat., 2010, 9, 205-213.

66. M. Sygletou, G. Kakavelakis, B. Paci, A. Generosi, E. Kymakis and E. Stratakis, ACS Appl. Mater. Interfaces, 2015.

67. G. D. Spyropoulos, M. M. Stylianakis, E. Stratakis and E. Kymakis, Appl. Phys. Lett., 2012, 100, 213904.

68. G. Kakavelakis, E. Stratakis and E. Kymakis, Chem. Commun., 2014, 50, 5285 – 5287.

69. G. Kakavelakis, E. Stratakis and E. Kymakis,, RSC Adv., 2013, 3 , 16288-16291.

5 Experiment

5.1 Materials preparation

Active blend

PCDTBT was purchased from Solaris and $PC_{71}BM$ was purchased from Solenne. Firstly, both of them were separately dissolved in dichlorobenzene: benzene (3:1) in a stirred hotplate at 80 ^{o}C overnight. To follow, the two solution were mixed for 3 hours on a stirred hotplate at 80 ^{o}C, creating the active blend of PCDTBT:$PC_{71}BM$ in ration 1:4.

Fig. 5.1 Materials and solution stirring.

Synthesis of surfactant-free Al NPs

For the synthesis of the NPs, a Pharos LASER was, which is a femtosecond pulse laser. For the experiment, the laser set up at 513 nm wavelength, 60 KHz repetition rate with pulse duration at 200 fs and power at 300 mW.

In particular, we use a mini glass container in which we place a quantity of our high purity metal Al. Then, we poure in the containers ethanol until the metal surface is covered up. The target should be moved during laser irradiation using a rotational mechanism to prevent laser pulses from irradiating the same spot (Fig. 5.2). This is important to improve reproducibility by reducing the influence of the inhomogeneousness of the surface structure of the target. The formation of NPs is in part brought about by the mechanical impact of plasma generated on the surface of the target.

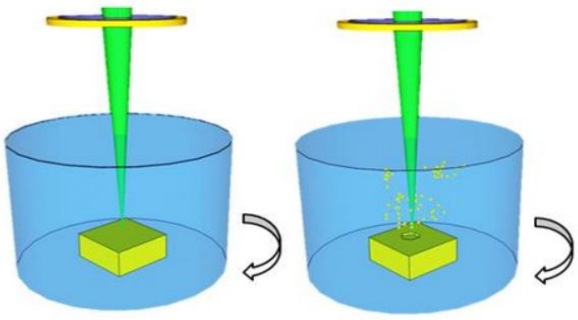

Fig. 5.2 Schematic illustration of laser-assisted production of surfactant-free NPs

Hole transport layer with Al NPs

PEDOT: PSS was filtered with filters 0.45 microns PVDF to remove any imperfection. Then, Al NPs (in Ethanol) were added in 350 μl PEDOT:PSS, creating solutions with different concentrations (0.6, 0.8 and 1%).

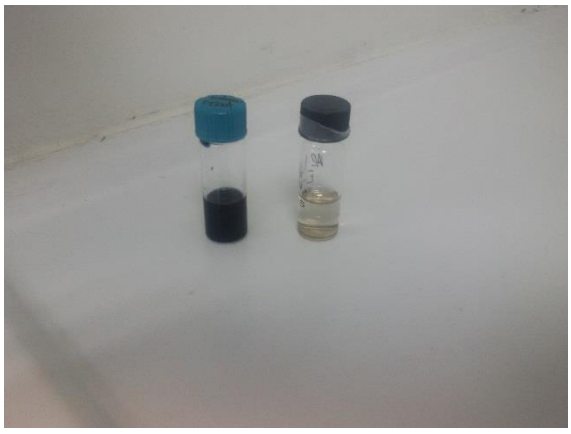

Fig. 5.3 PEDOT:PSS (left) and Al NPs in Ethanol (right).

5.2 Device fabrication

Cleaning of the substrates

Glass substrates coated with ITO and 20x15x1.1 mm size and with 6 different ITO electrodes were purchased from Luminescence Technology Corp. Each ITO electrode represents a different photovoltaic cell. The ITO layer is of 100 nm thickness and has a surface resistance of ~20 Ω/sq.

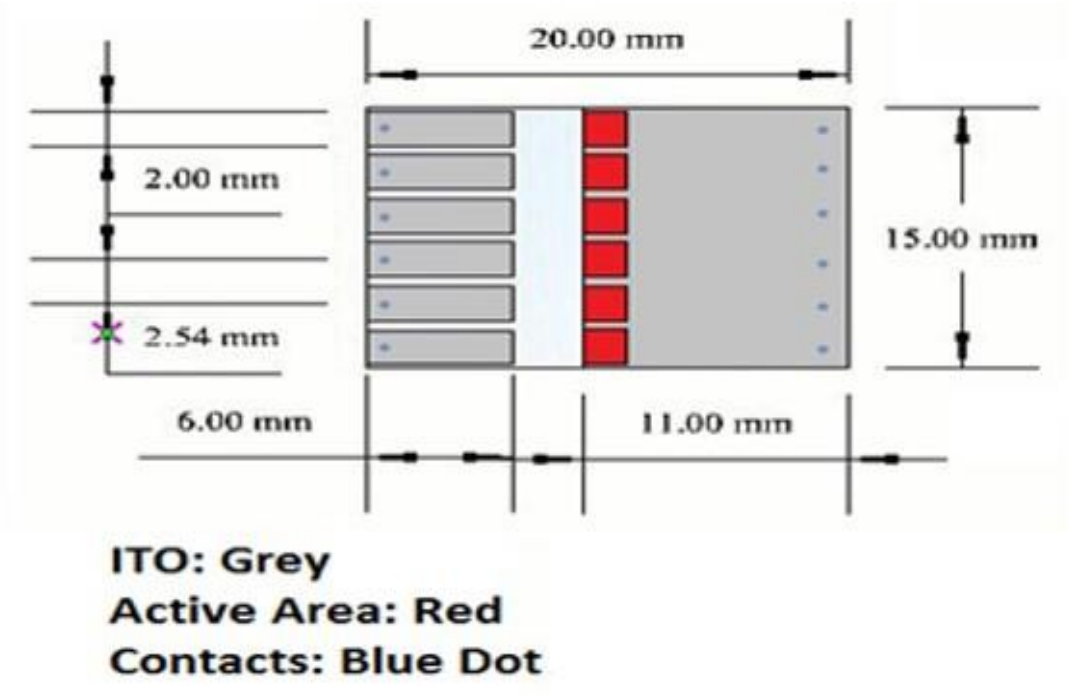

Fig. 5.4 Schematic drawing shows physical dimensions of patterned ITO glass.

The cleaning procedure is consisted from the following steps:

1) Placement of the substrates in soap-deionized water and in ultrasonic bath for 10 minutes.
2) Rinse with deionized water.
3) Placement in acetone and in ultrasonic bath for 10 minutes.
4) Placement in isopropanol and in ultrasonic bath for 10 minutes.
5) Transfer in Petri dish and in an oven at 120 ^{o}C for 15 minutes.
6) Finally in Ozone UV Cleaner for another 15 minutes.

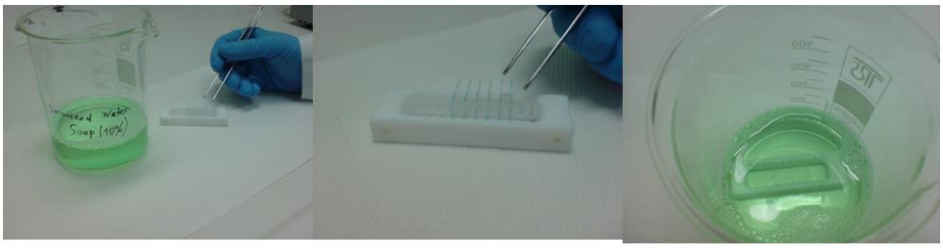

Fig. 5.5 Preparation for substrate cleaning.

Fig. 5.6 Substrates in ultrasonic bath.

Fig. 5.7 Placement of the substrates in oven.

Deposition of Hole transport layer

PEDOT:PSS assists by smoothing the surface of the ITO, produce better interlayer between the ITO & the active layer (energy match) and operates as a hole transport layer. Producing a high quality layer of PEDOT:PSS is of great importance for an efficient layout. For obtaining that, the surface to be coated must be very clean and hydrophilic. The cleaning procedure not only helps in cleaning but the use of the UV Cleaner improves the hydrophilicity of the surface.

PEDOT: PSS was purchased by HC Starck Clevios P AI 4083. Before deposition, it was filtered with filters 0.45 microns PVDF to remove any imperfection.

The deposition occurred by spin coating. Spin coating is a very simple and useful technique for deposition of thin uniform films on planar substrates (Fig. 5.8). The

solution is placed on the substrate, the substrate is rotated at an adjustable angular speed which results to the spreading of the liquid due to centripetal force. The rotation continues for a specific time. Both time and speed of the spin coating determine the amount of the solution that will remain on the substrate (and thus the thickness of the layer). Once the spin coating finishes, the sample allows to dry and then the procedure repeated with another solution (fabrication of the multilayer).

To avoid the possibility of Al NPs caving to the bottom of the solution, PEDOT:PSS with Al NPs were added in the ultrasonic bath for 1 minute before deposition, in order to make the solution homogenous.

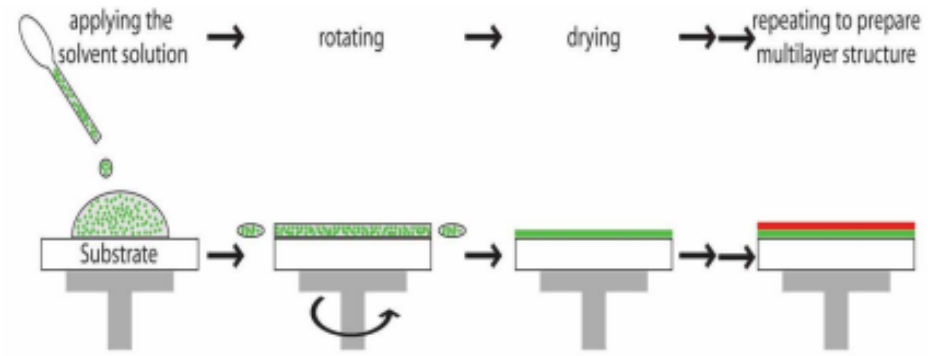

Fig. 5.8 Spin coated procedure

For the optimal layer, PEDOT:PSS should spin coated at 6000 rpm for 60 sec to achieve layer thickness of ~30 nm. To minimize the use of the material, only 30 μl were deposit on the substrate and to maximize the performance, samples with imperfection that can be observed with naked eye, were rejected.

Following the spin coating, a stripe at one edge and the cleaning of the ITO electrodes at the other edge of PEDOT:PSS layer of the substrate, swabbed with a cotton bud wetted with deionized water. These stripes are removed in order to ensure the contact with the ITO layer. The stripe represents the anode and the ITO electrode (where the cathode, aluminum, will be deposit) represents the cathode. The removal of PEDOT:PSS is very easy, since it is water soluble.

Finally, the substrates were placed in an oven at 120 ^{o}C for 15 minutes in order to remove any humidity residues. The whole procedure carried out outside glovebox since there was no infrastructure.

It is important to note that the exposure time of PEDOT:PSS in the air should be minimized because the performance deteriorates rapidly. The humidity of the atmosphere can lead to morphological changes due to the creation of an insulating layer on the surface of the HTL, which is rich in PS and aggravate the performance.

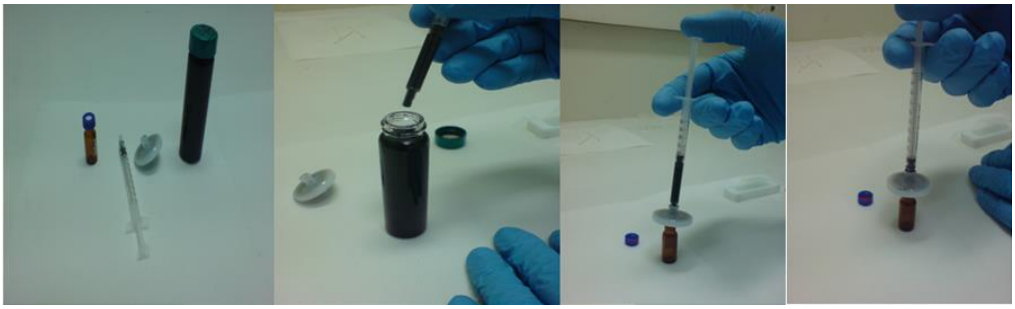

Fig. 5.9 PEDOT:PSS filtering process.

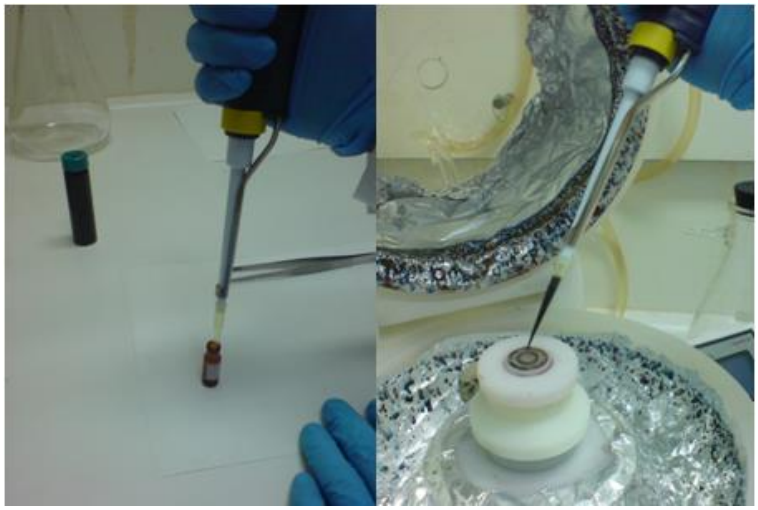

Fig. 5.10 Spin coating of HTL (PEDOT:PSS and PEDOT:PSS with Al NPs).

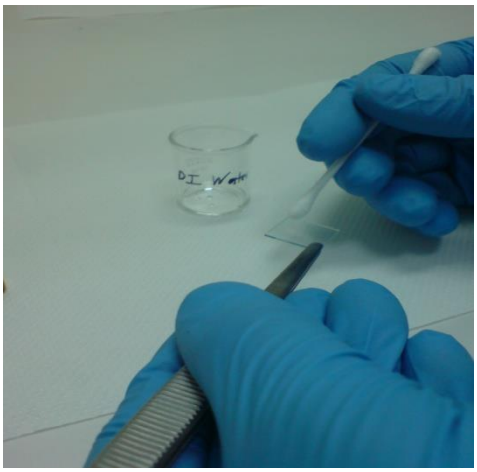

Fig. 5.11 Cleaning PEDOT:PSS with a cotton swab.

Deposition of Photoactive layer

The third step in the fabrication of organic photovoltaic device is the deposition of the active layer. After the preparation and before the deposition, the active blend was removed from the hotplate and relocate to a simple stirrer for 5 minutes. The active layer has thickness of 80 nm. To achieve that thickness, the blend was deposit on a spinning substrate at 1200 rpm for 110 seconds.

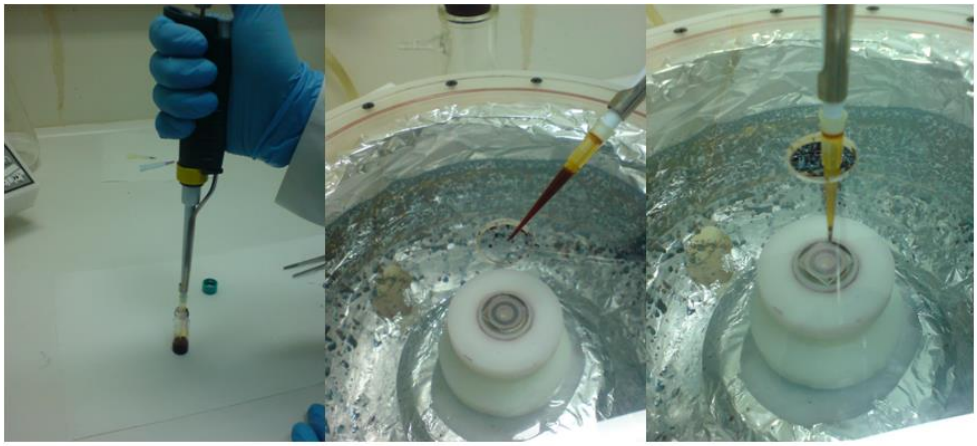

Fig. 5.12 Spin Coating of Active Layer.

After the deposition, the same etching was occurred as the PEDOT:PSS with a cotton bud wetted in chloroform until drying it.

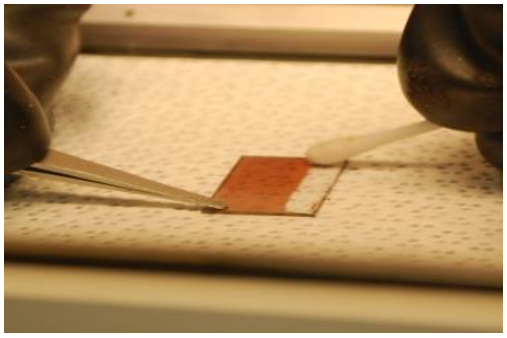

Fig. 5.13 Cleaning with a cotton swab

Thermal annealing

Thermal annealing applied to the device prior the deposition of the electron transport layer (ETL). Time and temperature are the two main factors in this process. In this device, the environment in which the annealing took place was important.

The thermal annealing for the PCDTBT:$PC_{71}BM$ took place in a glovebox on a hotplate at 80 ^{o}C for 3 minutes. This procedure increases the crystallinity of the active layer, which improves the absorption, hole mobilities and reduces carrier recombination.

Deposition of Electron transport layer

Another deposition technique is the vacuum thermal evaporation. In this procedure, pieces of the material we want to deposit, are placed in a cavity in a vacuum chamber. The substrate is located over the cavity in special mask on a rotated based. The cavity is supplied with current, due to resistance is heated and the material pieces melt and evaporate. The vaporized molecules overlay on the substrate and form the coating. The thickness depends on the distance between the substrate and the cavity and the heating time of the cavity.

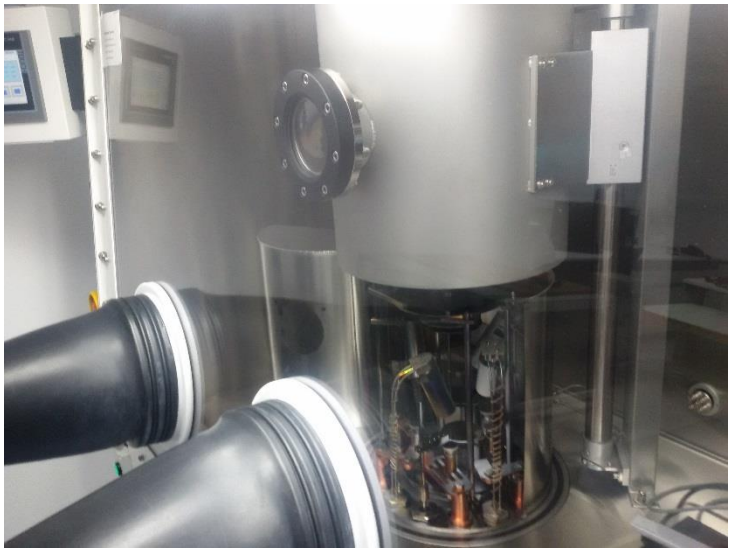

Fig. 5.14 Evaporator.

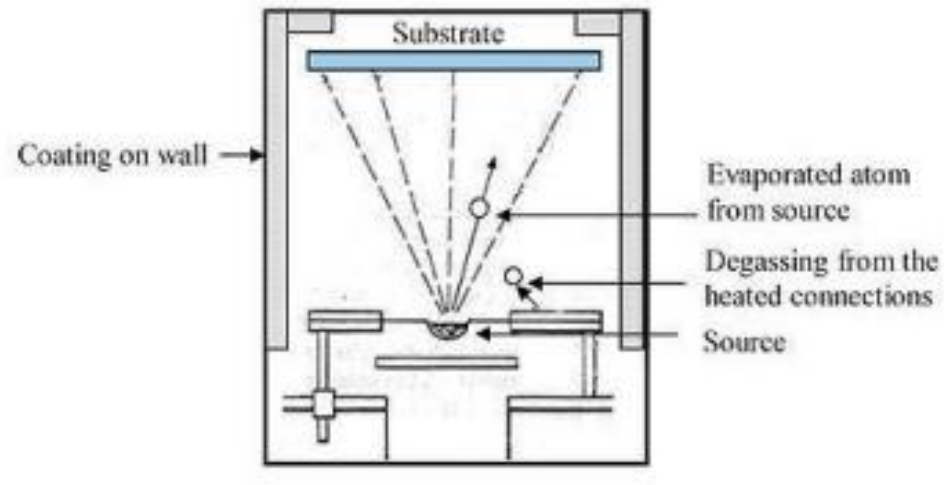

Fig. 5.15 Vacuum chamber

Ca is one of the materials used for the ETL. Different evaporations were tested to find the optimum thickness for the ETL. The best of them was at 5 nm with rate at 0.5 Å/sec on a spinning substrate.

The entire cathode evaporation procedure is described below:

(1) After the annealing of the active layer the samples are placed in a special mask whish exposes the area in which we want to deposit the Ca. Every sample is numbered in order to be distinguished. Afterwards, the mask is screwed on the arm of the vacuum chamber, in a specific distance from the cavity. Finally the cavity is filled with the amount of aluminum we desire.

(2) The chamber is sealed and the vacuum starts.

(3) As soon as the vacuum reaches 10^{-6} mbar the thermal evaporation can begin.

(4) We heat the thermal source until the sensor shows the desirable rate. Then we open the shutter in order to start the deposition on the substrate. When the desirable thickness achieved, the shutter and the thermal source are closed.

(5) After the vacuum reaches 10^{-6} mbar we start the deposition of the cathode.

Cathode deposition

Aluminum was the material we used for the deposition of the cathode. The procedure used for the deposition was the same of the ETL. The desirable rate for the deposition of Al was 1-1.5 Å/sec and the thickness was 100 nm.

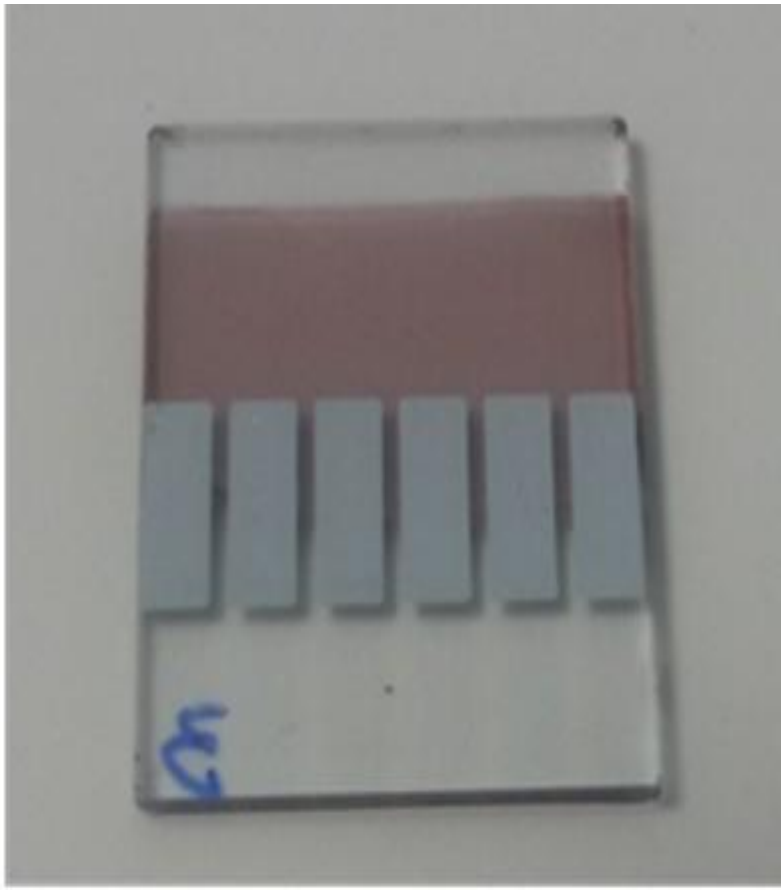

Fig. 5.16 Final device

It can be seen that aluminum cathode is deposited on the patterned ITO and not until the end of the substrate. The reason is to avoid direct contact with the probe, which can damage the cathode and shorted the device.

5.3 Device characterization

For the fundamental characterization, the current of the device as a function of applied voltage, under solar illumination simulation conditions, was measured. The voltage is applied from a voltage source and measurement of the current from a digital multimeter. These instruments are controlled by the computer B1500A (Semiconductor Device Analyzer) of Agilent Technologies. The software that is used

is Easy EXPERT. The main light source is a device simulation helium emission spectrum with equal illumination AM 1.5. The device was placed on a base, where the light ends via a mirror, the ITO side has been placed from the site of illumination entering.

Current-Voltage

After placed the device in a specific mask for this measurement, we measure the current density for each cell separately. The one electrode contacts the ITO at the upper side of the device and the other the ITO electrodes which are in contact with the Aluminum.

Afterwards, the lamp is turned on and the power is set in order to act as sun simulator (100mW/cm^2). From the Easy EXPERT program, we choose solar cell mode, then we set the active area of the solar cell, the range and the step voltage. Finally, we obtain the corresponding current-voltage curve. The algorithm of the program calculates important values for solar cells like current density (J) and short circuit current density (Jsc), open circuit voltage (Voc), fill factor (FF), cell efficiency (η%).

Finally the curves and the values which obtained by Easy Expert are processed by Origin Pro 8 where, useful curves also are designed (logarithmic, zoomed curves from J_{sc} to V_{oc}).

Other techniques

Another characterization is the quantum efficiency measurement. A solar cell's quantum efficiency value defines the photocurrent that the cell will produce when irradiated by photons of a particular wavelength. If the cell's quantum efficiency is integrated over the whole solar electromagnetic spectrum, one can evaluate the amount of current that the cell will produce when exposed to sunlight. The ratio between this energy-production value and the highest possible energy-production value for the cell (i.e., if the QE were 100% over the whole spectrum) defines the cell's overall energy conversion efficiency value. Note that in the event of multiple exciton generation (MEG), quantum efficiencies of greater than 100% may be achieved since the incident photons have more than twice the band gap energy and can create two or more electron-hole pairs per incident photon.

Two types of quantum efficiency of a solar cell are often considered:

1) *External Quantum Efficiency (EQE)* is the ratio of the number of charge carriers collected by the solar cell to the number of photons of a given energy shining on the solar cell from outside (incident photons).

2) *Internal Quantum Efficiency (IQE)* is the ratio of the number of charge carriers collected by the solar cell to the number of photons of a given energy that illuminate on the solar cell from outside and are absorbed by the cell.

The external quantum efficiency measurements were conducted immediately after device fabrication using an integrated system (Enlitech, Taiwan) and a lock-in amplifier with a current preamplifier under short-circuit conditions. The light spectrum was calibrated using a monocrystalline photodetector of known spectral response. The OPV devices were measured using a Xe lamp passing through a monochromator and an optical chopper at low frequencies (~200 Hz) in order to maximize the signal/noise (S/N) ratio.

Fig. 16 ECE measurement set up.

6 Results and discussion

OPV technology plays a major role in solar energy conversion technologies. Moreover, the architecture of bulk-heterojunction devices combines high absorption coefficient of the organic materials and the efficient generation of electron-hole in thin films.[70] however, to increase the device's efficiency, the thickness of the active layer must be reduced, but this leads to a decrease in the absorption of the BHJ film.[71]

One way to increase the efficient without changing the thickness is the introduction of the metallic nanoparticles. Metallic NPs can vitiate this balance by interesting properties (LSPR, SPP and scattering of light). Different metallic NPs (e.g. nanowires, nanospheres) have implanted in electrodes, in buffer layers, in active layer and between the interfaces.

6.1 Incorporation of surfactant free metallic NPs in HTL

The first report on performance enhancement via the incorporation of Au NPs into the PEDOT:PSS layer was by Chen et al..[72] The addition of Au NPs increased the exciton generation rate and the probability of exciton dissociation, thereby enhancing J_{sc} and fill factor (FF). An improvement of 20% was observed and was attributed to the local enhancement in the electromagnetic field due to the excitation of LSPR. More information was recently provided by Fung et al., who studied the electrical and optical properties of OPV cells with PEG-capped Au NPs embedded in the PEDOT:PSS layer. It was demonstrated that the absorption enhancement due to incorporation of Au NPs is insignificant and provides only a minor contribution to efficiency enhancement. This was postulated to be due to the lateral distribution feature of the strong near-field of plasmonic resonance around the metallic NPs. Considering electrical characteristics, they demonstrated that the incorporation of an appropriate amount of Au NPs reduces the resistance of the PEDOT:PSS layer. Moreover, there is an increase in the interfacial roughness between P3HT:PCBM and PEDOT:PSS after incorporation of Au NPs. The roughened interface contributes to the improvement of hole collection efficiency and leads to J_{sc} and FF enhancements.

To improve the OPV device characteristics, more research was made, incorporating not only Au NPs but also Ag. The reason for this enhancement was due to LSPR effect[73], but also on the light trapping effect by scattering incident light at wide angles.[74,75,76,77]

The incorporation of surfactant free Al NPs, produced by laser ablation method[44] is another promising approach, owing to their relative large diameter reaching tens of nm[45], combined with the high plasma frequency of Al.; the frequency, in which the electrons oscillate back and forth. The Al NPs can potentially lead to significantly greater performance enhancement than Ag or Au NPs, due to the much higher plasma

frequency of Al, which ensures a better overlap between plasmon resonance and absorption band of organic semiconductors. Al has a much higher plasma frequency ($3.57\ 10^{15}s^{-1}$) than Ag ($2.18\ 10^{15}s^{-1}$) and Au ($2.183\ 10^{15}s^{-1}$), which causes the Al NP enhancement peak to overlap well within the absorption spectrum of the photoactive layer PCPDTBT:C70-PCBM[78]. Therefore, the combination of high plasma frequency and large NPs diameter could give rise to enhanced light-trapping ability by efficient light scattering. In addition, the wide availability and low cost of Al provides a strong motivation for its utilization in plasmonic, rather than other noble NPs.

Furthermore, Al NPs have already been introduced into the active layer, achieving an efficiency improvement, as well as a lifetime increase of the OPV device.[79,80] It was found that the embedded Al NPs act as performance stabilizers, giving rise to enhanced structural stability of the active blend.[81]

Here, we report a facile method for the performance enhancement of OPV devices by blending Al NPs in the PEDOT:PSS HTL prior to spin coating. It was found that the incorporation of Al NPs into the PEDOT:PSS applied in Poly[N- 9′-heptadecanyl-2,7-carbazole-alt-5,5-(4′,7′-di-2-thienyl-2′,1′,3′-benzothiadiazole)]:Phenyl-C71-butyric acid methyl ester (PCDTBT:$PC_{71}BM$) based devices leads to a power conversion efficiency (PCE) improvement by 8.7 %. This enhancement can be attributed to light trapping by efficient scattering of incident photons (optical effect), as well as to enhanced conductivity (electrical effect) of the PEDOT:PSS HTL, resulting in enhanced hole mobility of the device, and therefore more efficient hole transport and collection. Since the Al NPs were added and not doped in the HTL in low concentrations the energy level of the PEDOT:PSS remained the same. Below, the TEM images and the absorption spectrum of the Al NPs, the pristine devices and the BHJ devices with Al NPs embedded in the HTL are shown (Fig. 6.1, 6.2 and 6.3 respectively).

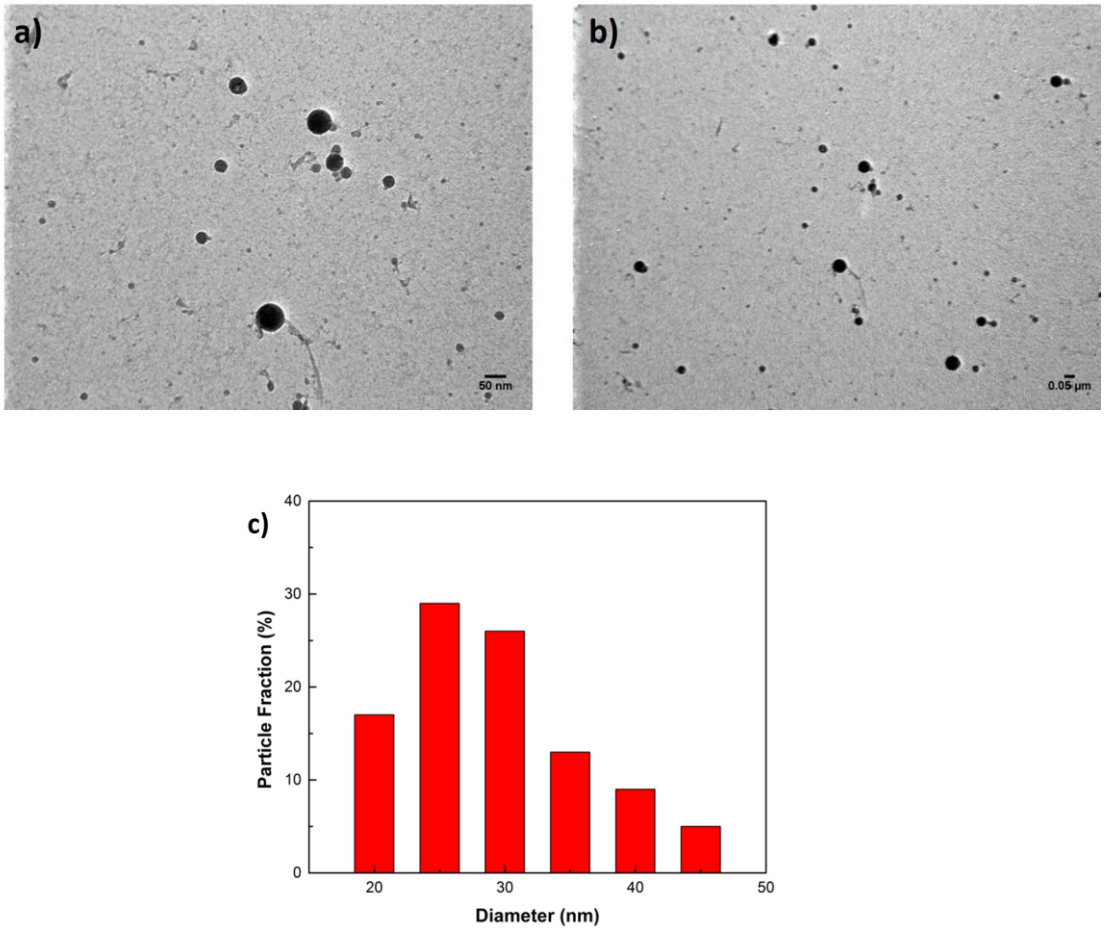

Fig. 6.1 TEM images of Al NPs and c) size distribution of the synthesized Al NPs.

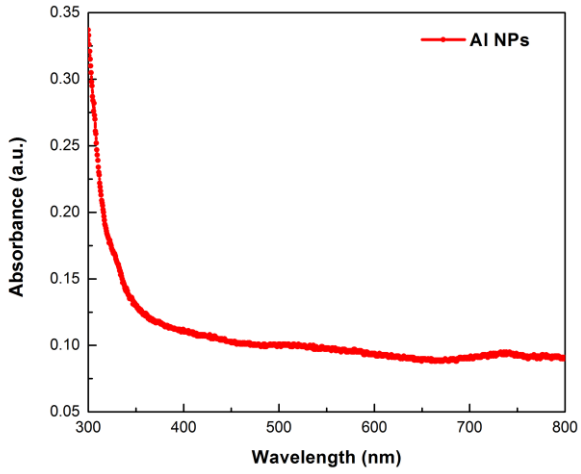

Fig. 6.2 Absorbance spectrum of the Al NPs.

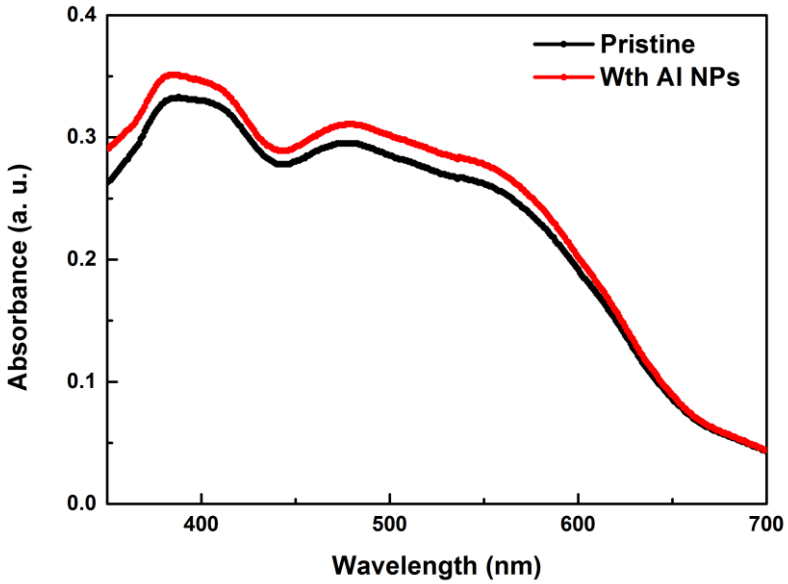

Fig. 6.3 Absorption spectrum of the pristine and Al doped devices.

The incorporation of Al NPs in our devices shows an incensement of the UV-Vis absorption spectra. Because the LSPR of Al NPs is in the UV region (Fig. 6.2), the improvement of the absorption can be attributed only due to light scattering of the Al NPs. Therefore, the Al NPs can act as an effective "optical reflector" for solar light; multiple reflections will cause the light to pass through the BHJ film several times.

Moreover, it is shown an improvement of short-circuit current density (J_{SC}) by 5 % whereas the open-circuit voltage (V_{OC}) and FF remain almost the same. The result is an increase by 8.7 % in the device efficiency (PCE) at the optimum Al NPs device with concentration of 0.8 % Al NPs in the PEDOT:PSS. Fig. 6.4 displays the J-V curves of the pristine device and the devices with different concentrations of Al NPs. The respective average characteristics are summarized in Table I.

Table I. Averaged photovoltaic characteristics of the devices with and without Al NPs inside the HTL.

	J_{SC} (mA/cm^2)	Calculated J_{SC} (mA/cm^2)	V_{OC} (V)	FF (%)	PCE (%)
PEDOT:PSS	10.92 ± 0.12	10.59	0.883 ± 0.010	60.0 ± 0.5	5.78 ± 0.12
PEDOT:PSS with 0.6 % Al NPs	11.33 ± 0.10		0.884 ± 0.020	60.0 ± 0.4	6.00 ± 0.12
PEDOT:PSS with 0.8 % Al NPs	11.47 ± 0.15	11.22	0.883 ± 0.020	62.0 ± 0.6	6.28 ± 0.16
PEDOT:PSS with 1 % Al NPs	11.13 ± 0.09		0.885 ± 0.010	59.6 ± 0.4	5.87 ± 0.09

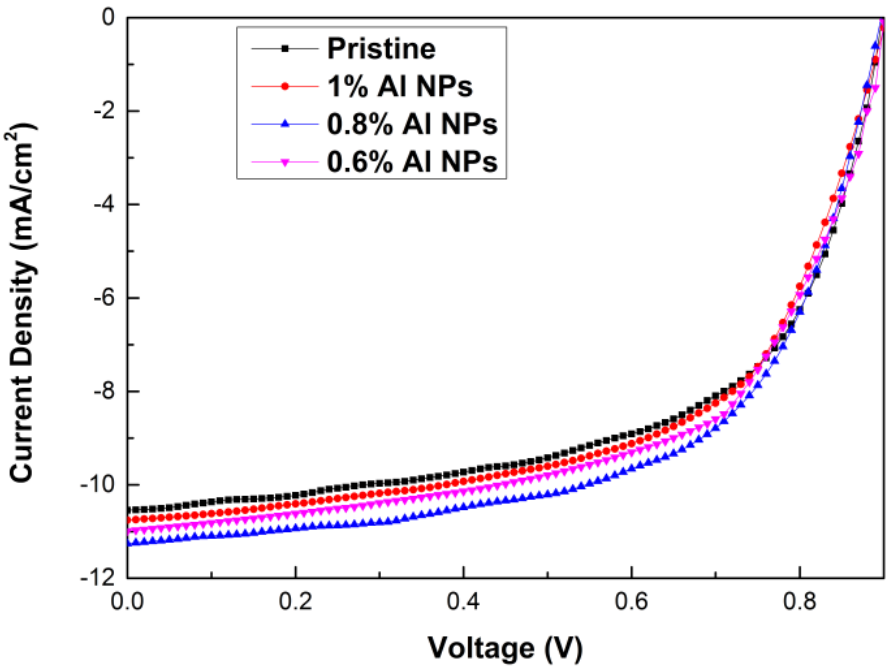

Fig. 6.4 J-V characteristics of the pristine and the OPV devices with Al NPs embedded in the HTL.

In order to have a clear evidence for the increased J_{SC} to the Al NPs incorporated devices, EQE spectra where collected. An almost broad and uniform increase in the entire wavelength rage is observed as shown in Fig. 6.5 indicating that the responsible

mechanism for the enhanced J_{SC} is the light trapping caused by the efficient scattering of the reflected photons through the ITO side. It should also be noted that the integrated J_{SC} values from the IPCE spectrum as presented in Table I for the pristine and the Al NPs based devices are 10.92 and 11.47 $mAcm^{-2}$ respectively for PCDTBT:PC_{71}BM. The IPCE calculated values are less than 4 % different than the actual measured Jsc values, indicating good accuracy of the OPV measurement.

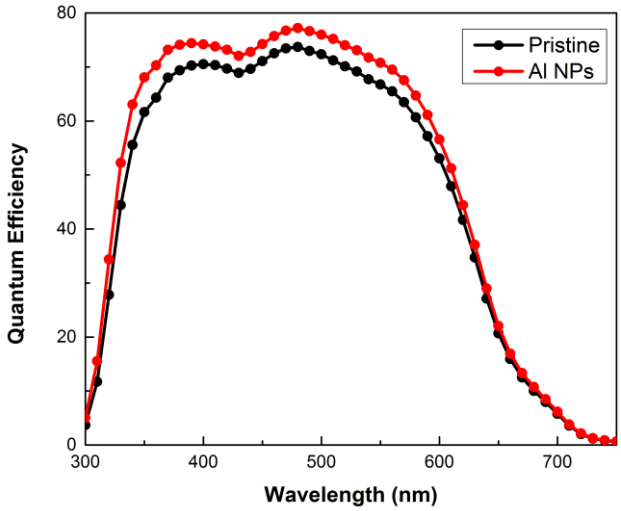

Fig. 6.5 Corresponding IPCE curves of the OPV devices with and without Al NPs (0.8 % concentration).

In order to confirm that the J_{SC} is increased due to better light harvesting in the active layer, caused by multiple scattering, the diffuse reflectance of the devices was recorded. Fig. 6.6 shows the diffuse reflectance spectra from 350-750 nm of the devices fabricated with and without Al nanoparticles in PCDTBT:PC_{71}BM. The lower reflectivity of the devices with NPs indicates stronger absorption than the pristine due to the scattering of large diameter Al NPs. By introducing Al NPs based reflectors inside the HTL, a significant fraction of transmitted photons from the active layer to ITO side are reflected back to the active layer and thus the possibility of the absorption inside the photoactive medium is increased, which in turn increases electron-hole pairs generation.[82]

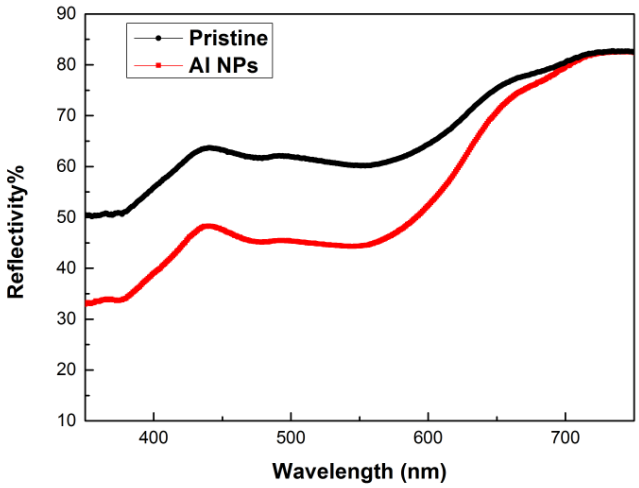

Fig. 6.6 Reflectance spectra of the pristine device and the device fabricated with the 0.8 % concentrations of Al NPs in the HTL.

Another point to be noted, is that, the conductivity of the PEDOT:PSS was notably enhanced upon the addition of Al NPs, as displayed in Table II, which results in an increase in the hole mobility of the PEDOT:PSS layer and thus the hole transport and collection ability of the device.[83] The conductivity data was obtained from the Hall-effect measurements (Ecopia HMS- 3000) in air based on the van der Pauw method, utilizing Ag paste on four corners of the pristine and Al doped PEDOT:PSS films as the electrodes.

Table II. Conductivity of the pristine and doped with Al NPs PEDOT:PSS films. Hole mobility of the OPV devices with and without Al NPs obtained by SCLC model

	Conductivity (S/cm)	**Hole Mobility (cm^2/Vs)**
PEDOT:PSS	5.086×10^{-4}	$(2.09 \pm 0.06) \times 10^{-5}$
PEDOT:PSS with 0.8 % Al NPs	8.953×10^{-3}	$(3.49 \pm 0.02) \times 10^{-5}$

Hole mobility measurements of the devices with and without Al NPs are depicted in Fig. 6.7. In order to investigate the responsible mechanism for PCE enhancement, as well as to show the observed enhancement conductivity of PEDOT:PSS, we studied the impact of Al NPs in hole mobility of the devices. We have fabricated hole-only diodes based on both pristine PEDOT:PSS and PEDOT:PSS doped with Al NPs using PCDTBT:$PC_{71}BM$, as photoactive layer. A thin layer of Au was thermally evaporated onto the active layer with thickness of ~20 nm. Calculations were based on Mott–Gurney equation (Space Charge Limited Current, SCLC) [Equation (23)]:

$$J = \frac{9}{8}\mu_h \varepsilon_o \varepsilon_r \frac{(V-V_{bi})^2}{L^3}, \textbf{(27)}$$

in which ε_r is the relative dielectric constant, ε_0 is the permittivity of free-space, μ_h is the charge carrier mobility, V is the applied voltage, V_{bi} the built-in potential and L is the thickness of the active layer. In Table II, hole mobility measurements of the devices with and without Al NPs are shown. The incorporation of Al NPs significantly improves hole mobility compared with the undoped device, leading to an improved hole transport and hole collection through the HTL.[84,85]

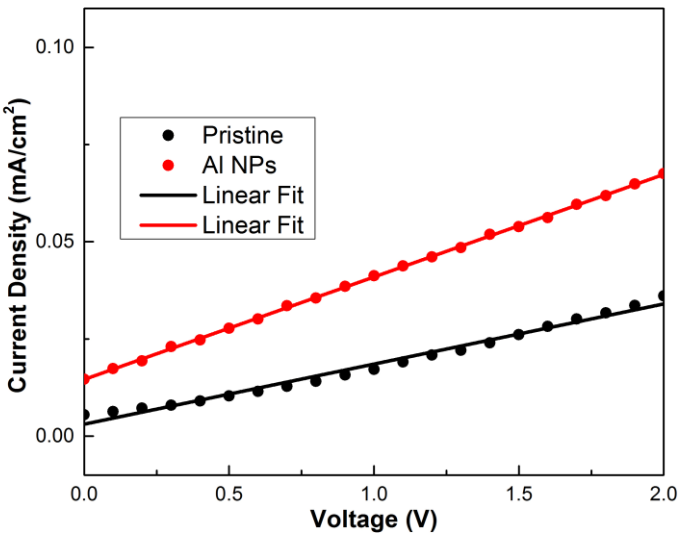

Fig. 6.7 hole mobility measurements of the pristine and the devices with Al NPs.

In Fig. 6.8, the AFM images of the PEDOT:PSS with and without the incorporation of the AL NPSs are displaced. The root-mean-squared (RMS)

roughness of PEDOT:PSS layer on ITO glass is measured to be 1.124 nm, while PEDOT:PSS mixed with Al NPs showing the RMS roughness slightly improved than the PEDOT:PSS layer (1.101 nm). This improvement helps the transfer of the holes from the active layer to the HTL, since there is less probability of deflecting the holes. This leads to an increase of the hole mobility, as confirmed by SCLC measurements.

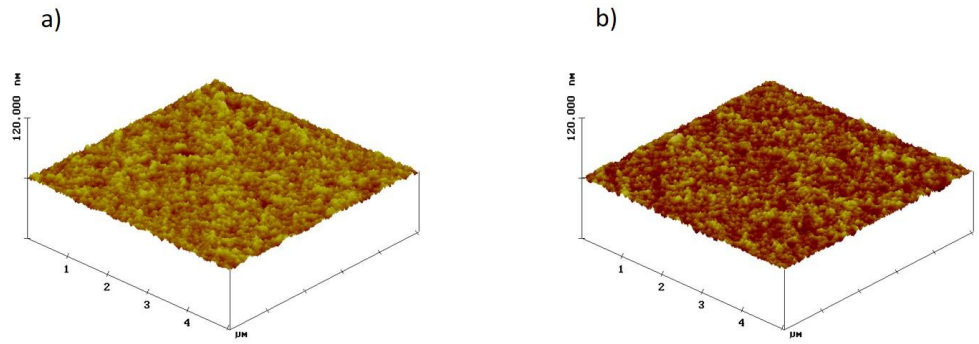

Fig. 6.8 AFM images of a) pristine PEDOT:PSS and b) PEDOT:PSS with Al NPs at 0.8 % concentration. The films were spin-coated on ITO glass sheets.

70. C. J. Brabec, S. Gowrisanker, J.J.M. Halls, D. Laird, S. Jia, S.P Williams, Adv. Mater. 22, 3839 (2010).

71. S. H. Park, A. Roy, S. Beaupr, S. Cho, N. Coates, J. S. Moon, D. Moses, M. Leclerc, K. Lee, A. J. Heeger, Nat. Photonics, 3, 297 (2009).

72. F. C. Chen, J. L. Wu, C. L. Lee, Y. Hong, C. H. Kuo, M. H. Huang, Appl. Phys. Lett. 95, 013305 (2009).

73. Q. Gan, F. J. Bartoli and Z. H. Kafafi, Adv. Mater., 2012, 25, 2385.

74. N. Kalfagiannis, P. G. Karagiannidis, C. Pitsalidis, N. T. Panagiotopoulos, C. Gravalidis, S. Kassavetis, P. Patsalas and S. Logothetidis, Sol. Energy Mater. Sol. Cells, 2012, 104, 165.

75. L. Qiao, D. Wang, L. Zuo, Y. Ye, J. Qian, H. Chen and S. He., Appl. Energy, 2011, 88, 848.

76. N. Kalfagiannis, P. G. Karagiannidis, C. Pitsalidis, N. Hastas, N. T. Panagiotopoulos, P. Patsalas and S. Logothetidis, Thin Sol. Films, 2014, 560, 27.

77. S. W. Tong, C. F. Zhang, C. Y. Jiang, G. Liu, Q. D. Ling, E. T. Kang, D. S. H. Chan and C. X. Zhu, Chem. Phys. Lett., 2008, 453, 73.

78. V. Kochergin, L. Neely, C.Y. Jao, and H. D. Robinson Appl. Phys. Lett., 2011, 98, 133305.

79. G. Kakavelakis, E. Stratakis and E. Kymakis, RSC Adv., 2013, 3, 16288.

80. G. Kakavelakis, E. Stratakis and E. Kymakis, Chem. Commun., 2014, 50, 5285.

81. M. Sygletou, G. Kakavelakis, B. Paci, A. Generosi, E. Kymakis and E. Stratakis, ACS Appl. Mater. Interfaces, 2015, DOI: 10.1021/acsami.5b03970.

82. J. W. Leem, S. Kim, S. H. Lee, J. A. Rogers, E. Kim and J. S. Yu, Adv. Energy Mater., 2014, 4, 1301315.

83. Z. Zhao, Q. Wu, F. Xia, X. Chen, Y. Liu, W. Zhang, J. Zhu, S. Dai and S. Yang, ACS Appl. Mater. Interfaces, 2015, 7, 1439.

84. D. D. S. Fung, L. Qiao, W. C. H. Choy, C. Wang, W. E. I. Sha, F. Xie and S. He, J. Mater. Chem., 2011, 21, 16349.

85. H. Kim, J. Lee, S. Ok and Y. Choe, Nanoscale Res. Lett., 2012, 7, 5.

7 Conclusion

To summarize, the incorporation of Al NPs into the HTL of an OPV device improves both its optical and electrical properties, leading to an efficiency enhancement of 8.7 % with an average PCE of 6.28 %. This efficiency improvement is primarily attributed to the effective light scattering of the incident photons, which increases the light path into the active layer. At the same time, the introduction of Al NPs into the HTL gives rise to an increase of its conductivity and, in turn, to an improvement of the hole transport ability. Moreover, the utilization of the most efficient donor polymer poly({4,8-bis[(2- ethylhexyl)oxy]benzo[1,2-b:4,5-b′]dithiophene-2,6-diyl}{3- fluoro-2-[(2-ethylhexyl) carbonyl]thieno [3,4-b] thiophenediyl}) (PTB7), instead of PCDTBT could lead to a further performance enhancement, since in this case the OPV device exhibits a broader absorption spectrum, which is expected to give rise to a significantly higher efficiency.

Publication/ Poster presentation

Krassas M., Kakavelakis G., Stylianakis M. M., Vaenas N., Stratakis E. and E. Kymakis, *Efficiency enhancement of organic photovoltaic devices by embedding uncapped Al nanoparticles in the hole transport layer*, RSC Advances, 2015, 5, 71704-71708.

Poster: Metal Nanoparticles in Organic Photovoltaic Applications, ISFOE 15, Thessaloniki 2015.